Effects of deglaciation on the crustal stress field and implications for endglacial faulting: A parametric study of simple Earth and ice models

Björn Lund

Department of Earth Sciences

Uppsala University, Sweden

March 2005

SKB

Effects of deglaciation on the crustal stress field and implications for endglacial faulting: A parametric study of simple Earth and ice models

Björn Lund
Department of Earth Sciences
Uppsala University, Sweden

March 2005

Abstract

The large faults of northern Scandinavia, hundreds of kilometres long and with offsets of more than 10 m, are inferred to be the result of major earthquakes triggered by the retreating ice sheet some 9,000 years ago. In this report we have studied a number of parameters involved in quantitative modelling of glacial isostatic adjustment (GIA) in order to illustrate how they affect stress, displacement and fault stability during deglaciation.

Using a variety of reference models, we have verified that our modelling approach, a finite element analysis scheme with proper adjustments for the requirements of GIA modelling, performs satisfactory. The size of the model and the density of the grid have been investigated in order to be able to perform high resolution modelling in reasonable time.

This report includes studies of both the ice and earth models. We have seen that the steeper the ice edge is, the more concentrated is the deformation around the edge and consequently shear stress localizes with high magnitudes around the ice edge. The temporal evolution of height and basal extent of the ice is very important for the response of the earth model, and we have shown that the last stages of ice retreat can cause fault instability over a large lateral region.

The effect on shear stress and vertical displacement by variations in Earth model parameters such as stiffness, viscosity, density, compressibility and layer thickness was investigated. More complicated geometries, such as multiple layers and lateral layer thickness variations, were also studied. We generally find that these variations have more effect on the shear stress distributions than on the vertical displacement distributions. We also note that shear stress magnitude is affected more than the spatial shape of the shear stress distribution.

Fault stability during glaciation/deglaciation was investigated by two different variations on the Mohr-Coulomb failure criterion. The stability of a fault in a stress field is assessed by the Instability measure, simply the difference between the shear stress magnitude on a fault plane and the normal stress times the coefficient of friction. The differential Fault Stability Measure, dFSM, /Wu and Hasegawa, 1996a/ is a relative measure which assesses whether or not a fault becomes more unstable when the stress state changes. We show that dFSM must be cautiously interpreted with respect to the initial state whereas Instability has a more direct interpretation. We also show that the initial state of stress is very important for the assessment of fault stability during glacial rebound and has to be chosen with care.

List of important variables and abbreviations:

S_{ij}, σ_{ij}, σ_n	Stress tensor, effective stress tensor, normal stress.
σ_1, σ_2, σ_3, S_1, S_2, S_3	Maximum, intermediate and minimum principal stress.
S_H, S_h, S_V	Maximum and minimum horizontal stress, vertical stress.
τ, S_0	Shear stress, cohesion.
u_i	Displacement.
ρ	Density.
g	Gravitational acceleration.
p, P, P_f	Pressure, pressure, pore fluid pressure.
μ	Coefficient of friction, except in section 2.2.1 where it is the shear modulus.
ν	Poisson's ratio.
η	Viscosity.
E	Young's modulus.
GIA	Glacial isostatic adjustment.
LGM	Last glacial maximum.
EOG	End of glaciation.
dFSM	Differential fault stability margin.

Contents

1   Introduction

The identification of large neotectonic faults in northern Scandinavia as endglacial features /Kujansuu, 1964; Lagerbäck, 1979; Olesen, 1988/, most likely the result of very large earthquakes at the time of deglaciation, has prompted an increasing number of investigations into the mechanisms responsible for these events. The primary component of any such investigation is Glacial Isostatic Adjustment (GIA) theory, which describes the response of the Earth to loading events such as a glaciation/deglaciation sequence. Modern GIA investigations initiated with /Peltier, 1974/ and /Farrell and Clarke, 1976/ and GIA theory has evolved to include the effects of sea-level change, Earth rotation etc /e.g. Wu and Peltier, 1982; Mitrovica et al. 1994a; Milne et al. 1999; Mitrovica et al. 2001/. The three dimensional effects of the ice sheet is usually included in these model /e.g. Tushingham and Peltier, 1991; Mitrovica et al. 1994b; Lambeck et al. 1998a/ whereas the Earth models generally only vary in the radial direction. Fully three dimensional formulations of the theory is still only starting to evolve, e.g. /Cadek, 2003/.

The models above are all analytical or semi-analytical. In order to study the fully three dimensional problem, i.e. 3D Earth models, it is currently necessary to utilize fully numerical procedures, such as finite element analysis, FEA. Early, rather coarse, FE models such as those by /Gasperini and Sabadini, 1989/ and /Wu, 1992/ have now evolved into full fledged 3D analyzes /e.g. Wu et al. 1998; Kaufmann et al. 2000; Kaufmann and Wu, 2002/. These models are all flat-earth approximations, excluding all gravitational contributions to the GIA problem. Much effort has lately been directed toward the development of spherical FE models including the gravitational effects, e.g. /Latychev et al. 2003/ and /Wu and van der Wal, 2003/.

The processes underlying the stress accumulation necessary to create the large endglacial faults of northern Scandinavia has been studied by a large number of authors. As this report only considers the response of generic GIA models and not specific, northern Scandinavian models, we will concentrate here on studies of faulting based crustal stresses from quantitative GIA models. Early investigations /Walcott, 1970; Stein et al. 1979/ found that postglacial rebound stresses alone could be responsible for the mode of earthquake failure in eastern Canada. /Quinlan, 1984/ pointed out that the rebound stress probably rather acts a triggering mechanism for faults close to failure in the ambient tectonic stress field. The models used in these studies were elastic plates on fluid mantles, neglecting the effect of stress relaxation in a viscoelastic medium. /Johnston, 1987, 1989/ showed that earthquakes are suppressed by large ice sheets and discussed strain accumulation under the ice sheets but did not consider rebound stresses. /James and Bent, 1994/ calculated rebound strain rates in a viscoelastic model and found that they were greater than current seismic strain rates in Canada, implying that rebound alone could cause the earthquakes. During the last decade, Wu with others has presented a number of studies on fault stability during glaciation and deglaciation, both basic, generic models /Wu and Hasegawa, 1996a; Johnston et al. 1998/ as well as applied to Canada /Wu and Hasegawa, 1996b; Wu, 1997; Wu and Johnston, 2000/ and Fennoscandia /Johnston et al. 1998; Wu et al. 1999/. These are all viscoelastic models which use the difference in Fault Stability Margin, dFSM, /Quinlan, 1984/ to infer increased/decreased fault stability, see below for details. dFSM was also used by /Klemann and Wolf, 1999/ as one of a number of parameters in their study of the implications of a ductile layer in the crust for the deformation caused by the Fennoscandian ice sheet.

These studies generally find that earthquake activity is suppressed by the emplacement of the ice sheet but greatly enhanced at the end of deglaciation. The onset and location of increased fault instability, however, varies with ice sheet dimension and temporal evolution, lithospheric and mantle structure and the initial state of stress.

The purpose of this report is to set the stage for an in-depth investigation of the mechanisms responsible for the large endglacial faults in northern Scandinavia. In order to achieve this, we will;

- Set up and validate a generic, finite element, GIA model (chapter 2).

- Study the influence of element size and model extent on the resulting stress and displacement fields (chapter 3).

- Vary the physical properties of the Earth model, in order to gain insight into the relative importance of these parameters on the crustal stress state (chapter 4).

- Investigate large scale Earth model variations, such as multiple layering and lateral variation in elastic and viscous properties (chapters 5 and 6).

- Study various ice models (chapter 7).

- Introduce an absolute fault stability measure and study how this and the dFSM fault stability measure are affected by variations in initial stress state and pore pressure (chapter 8).

2   Modelling glacial isostatic adjustment

This section describes the assumptions we make in order to simplify the equations governing the loading of a viscoelastic Earth, and the implementation of these equations in a finite element context. We also present the results of benchmark tests.

2.1   Governing equations and finite element analysis

Due to the presence of an initial stress field in the Earth, the equations governing stress and displacement in a viscoelastic, layered medium, in response to a surface load are usually expressed as perturbations from a pre-existing equilibrium state. The necessary equations are the incremental momentum balance, the incremental continuity equation and the incremental constitutive equation. Most finite element packages correctly handle the continuity and constitutive equations and we will therefore not consider these here.

The material incremental momentum equation for quasi-static, infinitesimal perturbations of a stratified, compressible, fluid Earth initially in hydrostatic equilibrium subject to gravitational forces but neglecting inertial forces is /e.g. Wolf, 1991; Johnston et al. 1998/:

$$\sigma_{ij,j}^{\delta} + (p_{,j}^{0} u_j)_{,i} + \rho^{\Delta} g_i^{0} + \rho^{0} g_i^{\Delta} = 0 \qquad (1)$$

where σ is the Cauchy stress tensor defined as positive in tension, $p = -\sigma_{kk}/3$ is the pressure, ρ the density, g the gravitational acceleration and u the displacement. The superscripts 0, δ and Δ denote the initial, material incremental and local incremental fields respectively. The usual summation and differentiation conventions apply to the index notation. The first term in Eq 1 describes the force from spatial gradients in stress. The second term concerns the incremental stress resulting from a particle's displacement in the initial stress field, parallel to the stress gradient. This term is commonly referred to as "pre-stress advection". The third and fourth term describe perturbations to the gravitational forces due to changes in density and gravitational acceleration, respectively. The third term is sometimes referred to as the buoyancy term, which, together with the second term, accounts for isostacy.

The momentum equation is frequently simplified by ignoring the change in the gravitational field within the material, i.e. neglecting the fourth term in Eq 1. This term is only significant at the very longest wavelengths and models which ignore this incremental gravitational force, IGF, are usually described as non-self-gravitating. The effect of this approximation was discussed by /Amelung and Wolf, 1994/, who showed that the two approximations of ignoring the IGF term and the sphericity of the Earth, i.e. using a flat-earth model, largely compensate each other.

Further simplification is obtained for layers that are uniform in density and incompressible. In such layers there is no change in density with deformation and therefore the third term in Eq 1 vanishes. For a non-self-gravitating incompressible Earth the momentum equation can be rewritten in terms of the local incremental stress as:

$$\sigma_{ij,j}^{\Delta} = 0, \qquad \sigma^{\Delta} = \sigma_{ij}^{\delta} + p_{,k}^{0} u_k \delta_{ij} = \sigma_{ij}^{\delta} + \rho^{0} g^{0} u_k \delta_{ij} = 0. \qquad (2)$$

We will use this simplified equation for the finite element modelling.

The viscoelastic materials in our models are implemented using linear Maxwell viscoelasticity, which, although very simple, has provided a reasonable fit to a variety of GIA data.

2.1.1 Implementation of the viscoelastodynamic equations into finite element codes

We are indebted to Prof Wu for invaluable help on the implementation of the simplified viscoelastodynamic momentum equation into Abaqus, our commercial finite element analysis package. The following paragraphs are based on discussions with Prof Wu, and an early manuscript of /Wu, 2004/.

Most commercial finite element packages are mainly designed for engineering applications where only the divergence of the stress tensor is included in the momentum equation, $S_{ij,j} = 0$, ignoring isostacy and self-gravitation. This makes the modelling codes unsuitable for geophysical applications involving long wavelengths and non-elastic deformation /Wu, 1992/. If we, however, consider our model as non-self-gravitating and the elements as incompressible and uniform in density, we can utilize Eq 2 to define a new, finite element stress tensor as

$$S^{FE} = S - \rho^0 g^0 u_z I \tag{3}$$

where u_z is the displacement in the vertical direction, parallel to the gravity field, and I is the identity matrix. Differentiation gives us

$$S^{FE}_{ij,j} = S_{ij,j} - \rho^0 g^0 u_{z,j} \delta_{ij} = 0 \tag{4}$$

which is the momentum equation we desire, expressed in terms of the new stress. Due to the transformation in Eq 3, new boundary conditions must be applied to the finite elements. In the following, P is the surface load, the index h signifies a horizontal coordinate and $[F]^{+Z}_{-Z} = lim_{\epsilon \to 0} (F(Z+\epsilon) - F(Z-\epsilon))$.

1. At the Earth's surface: $[S^{FE}_{zz} + \rho^0 g^0 u_z]_{z=0} = P$, assuming the density of air to be zero, and $[S^{FE}_{hz}]_{z=0} = 0$.

2. At solid-solid interfaces at depth Z: $[S^{FE}_{zz}]^{+Z}_{-Z} = (\rho^0_{+Z} - \rho^0_{-Z})g^0 u_z$ and $[S^{FE}_{hz}]^{+Z}_{-Z} = [u_h]^{+Z}_{-Z} = [u_z]^{+Z}_{-Z} = 0$.

These boundary conditions are easily implemented in finite element packages as Winkler, or elastic, foundations with spring constants $\rho^0 g^0$ or $(\rho^0_{+Z} - \rho^0_{-Z})g^0$, respectively. All non-vertical material interfaces where density is changing should have these foundations attached.

Finally, due to the transformation in Eq 3, the stress output after a finite element model run has to be converted back to the "correct" stress through $S = S^{FE} + \rho^0 g^0 u_z I$. This conversion is crucial since stress magnitudes otherwise will be much too low. Displacements in the finite element model are not affected by the transformation and, therefore, need no postprocessing.

2.2   Validation of the finite element implementation

We implemented the Winkler foundation formalism discussed above in our finite element package Abaqus and performed a number of benchmark tests. It is surprisingly difficult to find good benchmark tests where there is data available on both displacements and stress. We will discuss four benchmarks below, all varying in earth and ice models as well as presented output. We divide our validation process into two classes of models, two-dimensional models (the ice sheet as a loaf of bread) and axisymmetric models (a hockey puck ice cap). Our models below all have an interior area of high resolution approximately 4,000×900 km, horizontally×vertically, increasing element size away from the interior out to 10,000×5,000 km (usually 10 and 5 times the ice load radius/lateral extent) and infinite elements to the sides and at the bottom.

2.2.1   Two-dimensional models

Viscoelastic half-space in 2D with an impulsive boxcar load

The solution for the response of a Maxwell viscoelastic half-space to an impulsive boxcar load with uniform amplitude is well known /e.g. Wolf, 1985/. The vertical displacement at the surface is given in the wave-number domain by

$$\int_{\infty}^{-\infty} \frac{-PL(k)}{\rho g + 2\mu k} \left[1 + \frac{2\mu k}{\rho g}\left(1 - e^{-\alpha t}\right)\right]e^{ikx} \, dk \tag{5}$$

where P is the amplitude of the boxcar load and L(k) its wave-number k domain representation. μ is the shear modulus, t is time and x horizontal distance. α is the relaxation time given by

$$\alpha = \frac{\rho g \mu}{\eta(\rho g + 2\mu k)}. \tag{6}$$

We evaluated Eq 5 numerically using a Fast Fourier Transform (FFT) and compared our finite element calculations to the FFT result. Figure 2-1 shows the comparison of the two methods for a 15 MPa 2D boxcar load with 1,000 km half-length applied to a 2D, incompressible, non-self-gravitating viscoelastic half-space with the following parameters:

Density: 5,000 kg/m^3.

Young's modulus: 113 GPa.

Viscosity: 1.45×10^{21} Pa s.

Poisson's ratio: 0.5.

As Figure 2-1 shows, the two methods agree extremely well for the vertical surface displacements. The largest discrepancies are at the ice edge at longer times when the stress gradient becomes too steep for the used finite element grid. As pointed out by /Wu, 1992/, this is not a problem in realistic calculations since there will always be an elastic layer on top of the viscoelastic half-space that removes the discontinuity. A similar viscoelastic half-space model with impulsive boxcar loading is presented by /Wu, 1992/ where he plots both vertical displacements and Mises stress. Implementing that model in our finite element scheme we obtain results that agree very well with those of /Wu, 1992/ for both variables.
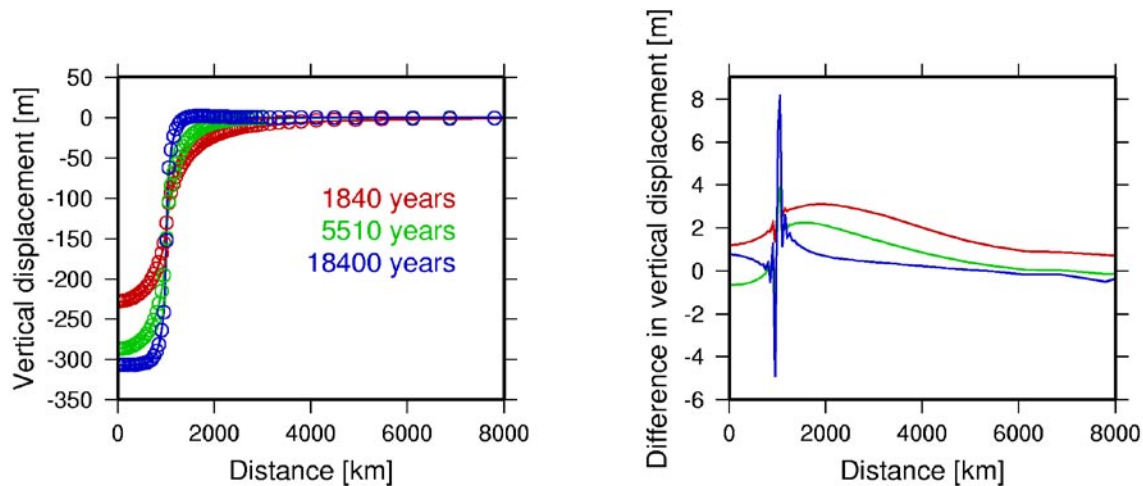
Figure 2-1. *Vertical surface displacement of a viscoelastic half-space subject to a 1,000 km impulsive boxcar load. Lines are finite element modelling results and circles are results from the transform method. Times are years after the application of the load. The right plot show the difference between the transform method and the FE method.*

2.2.2 Axisymmetric models

Axisymmetric viscoelastic half-space with a boxcar Heaviside load

Using a very similar setup as in the 2D case above, we compared our finite element model of an axisymmetric Maxwell viscoelastic half-space subject to an impulsive boxcar load with that of /Wu, 1993/. The results for vertical surface displacements again agree very well. This comparison is strictly visual from the results in /Wu, 1993/.

Elastic plate overlying a viscoelastic half-space

The papers by /Klemann and Wolf, 1998, 1999/ present shear stress and stress state results of their spectral GIA models. These models are ideal validation models for our finite element implementation since they are also incompressible, non-self-gravitating models. We tested our technique against the results of /Klemann and Wolf, 1998/. The tested model is an axisymmetric model with an elastic plate overlying a Maxwell viscoelastic half-space. The model is subjected to an ice load of elliptic cross-section, 2.8 km high at the center with radius 900 km and a density of 0.91 kg/m^3, giving a maximum pressure of 25 MPa below the center of the ice. The loading history is a simplified representation of the final Weichselian glaciation in Fennoscandia, the load is linearly increased over 90 kyr to its maximum, referred to as the Last Glacial Maximum (LGM), and then linearly decreased to zero over 10 kyr, End of Glaciation (EoG). The model is run for an additional 8 kyr up to the present time. Note that the ice sheet all through its history occupies the full 900 km radius, it is only the height of the ice that varies with time. Parameters of the model are shown in Table 2-1.

Table 2-1. Parameters for model tested agaist /Klemann and Wolf, 1998/.

	Elastic plate	Half-space
Thickness	100 km	∞
Density	3,380 kg/m^3	3,380 kg/m^3
Young's modulus	192 GPa	435 GPa
Viscosity	∞	1.0E+21 Pa s
Poisson's ratio	0.5	0.5
Gravity	9.81 m/s^2	9.81 m/s^2

Figure 2-2 shows the result of our modelling, in terms of the maximum shear stress $(\sigma_1-\sigma_3)/2$ and the state of stress, calculated using only the modelled incremental rebound stresses without overburden or other additional stresses. Comparing to the figures in /Klemann and Wolf, 1998/, see Figure 2-3, the results are remarkably similar. We were unfortunately unable to obtain the numerical values /Klemann, personal communication 2004/ for the model for a quantitative comparison. Maximum shear stress contours agree both in shape and numerically and the stress states are very similar. The slight differences in the results could depend on the relative grid spacing of the models and the averaging procedures used in the presentation of the data. In order to obtain the best resolution possible, our test model had a very dense grid with a total of 721,731 elements, requiring almost 3.5 GB of computer memory and 7 hours of computing time on a HP zx6000 with dual Itanium2 1.5 GHz processors.
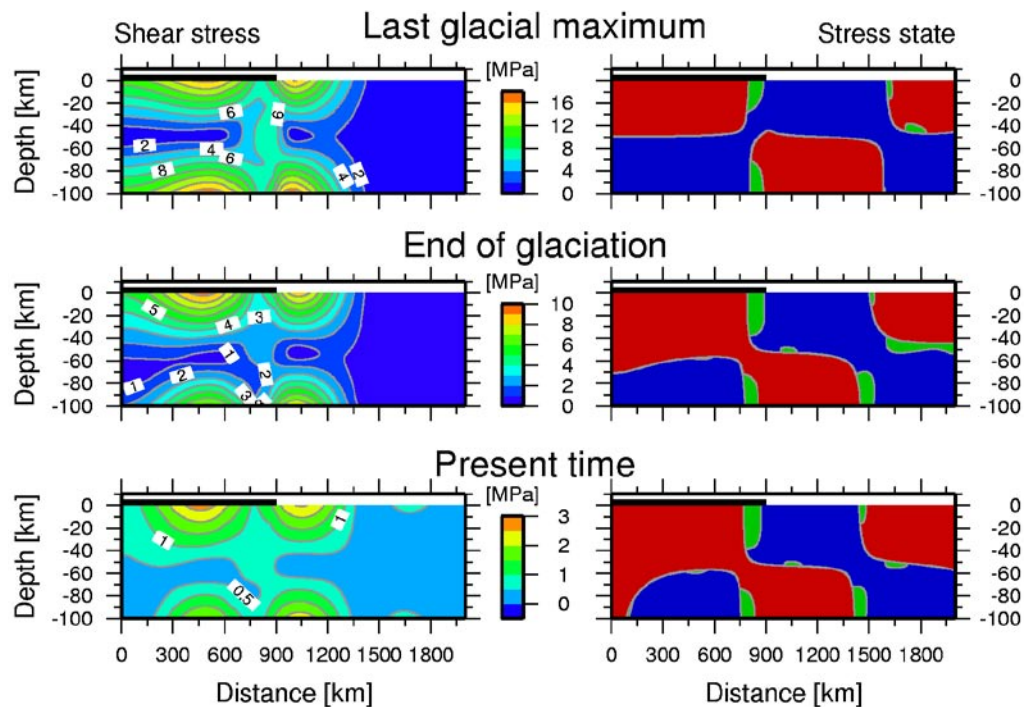
Figure 2-2. *Maximum shear stress and the state of stress in the model after /Klemann and Wolf, 1998/ at three different times. At LGM the full ice load is on the model, 10 kyr later at EoG the ice has melted and Present is additionally 8 kyr later. The extent of the ice load at LGM is indicated by a black bar on top of the plots. Maximum shear stress contours in MPa, stress states are coloured as; extension (blue), strike-slip (green) and thrust (red).*
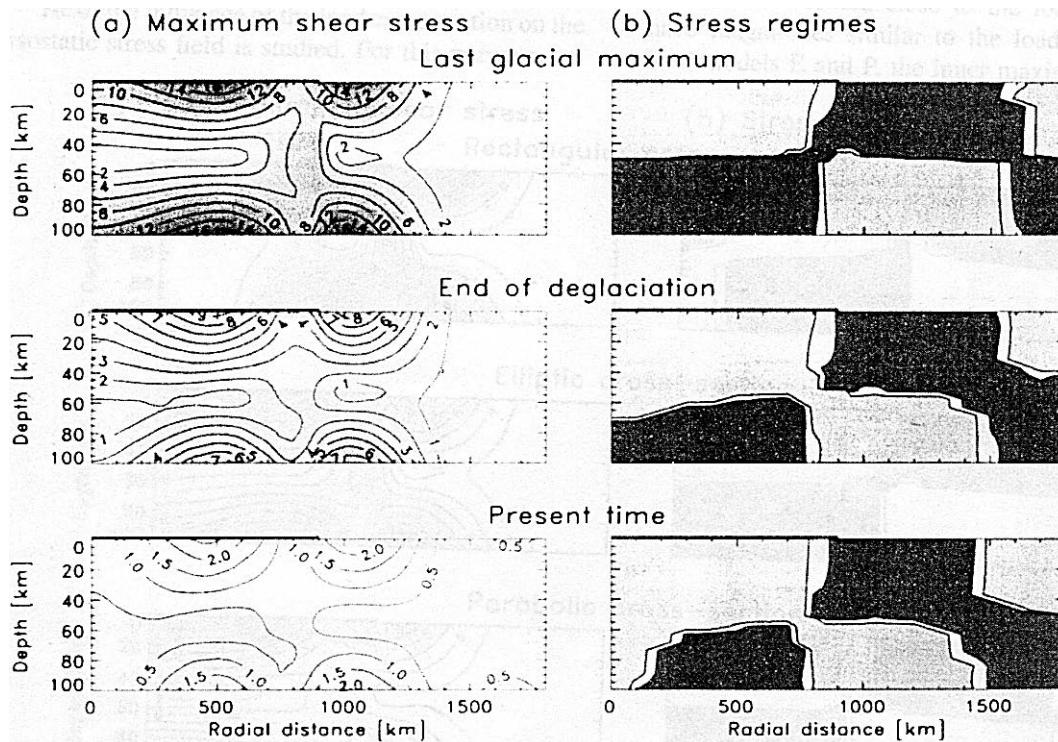
Figure 2-3. /Klemann and Wolf, 1998/ results for the model discussed above. Parameters as in Figure 2-2, except that the stress regimes here are indicated as; extension (black), strike-slip (white) and thrust (grey).

Radially variable Earth model

The Geodynamics group at the Research School of Earth Sciences, Australian National University (ANU), Canberra, Australia, maintains a web site with a number of benchmark tests /Kaufmann and Johnston, 1997/ for models of glacial isostatic adjustment. The benchmarks are intended for spherical, self-gravitating, Earth models, computed by spectral methods, but we have adopted the simplest model for testing with our flat-earth, non-self-gravitating, finite element method. The presented outputs of the benchmarks, relevant to us, are vertical and horizontal displacements at the model surface. There are, unfortunately, no stress results available. The Earth model we adopt, Earth 2a /Kaufmann and Johnston, 1997/, is a layered, incompressible model with a 70 km elastic "lithosphere" overlying a three-layered, viscoelastic mantle on top of a fluid core. The model uses elastic parameters from the Preliminary Reference Earth Model (PREM) /Dziewonski and Anderson, 1981/, volume-averaged over each of the four layers, and a simple viscosity distribution, see Table 2-2.

Table 2-2. Parameters used in the PREM model.

Depth, km	0–70	70–420	420–670	670–2,891
Density, kg/m^3	3,037	3,438	3,871	4,978
Shear modulus, GPa	50.61	70.36	105.49	228.34
Viscosity, Pa s	∞	7.00E+020	7.00E+020	7.00E+021

14

The ice model is a simple disc with rectangular cross-section, 800 km radius, 1 km height and a density of 1,000 kg/m³. It is a Heaviside loading history and the model is evaluated after 0, 1, 2, 5, 10, and 110 kyr (simulating infinity) after loading. We implement a flat, axisymmetric model in order to come as close as possible to the spherical case. Our results for the vertical displacements agree very well with the spectral results, see Figure 2-4, allowing for the fact that we used 110 kyr instead of infinite time. The horizontal displacements, however, are less in agreement. It seems that our horizontals evolve faster in time than the benchmarks, and do not reach the same positive distance but instead decline to larger negative distances. The overall shapes of the distributions agree rather well, however, with a minimum at the edge of the ice sheet and an asymmetric distribution. It is currently unclear to us what the discrepancy is due to, it could be that our implementation ignores the fluid outer core below 2,891 km depth, or it is perhaps a result of the non-self-gravitating, flat-earth approximations. It is interesting to note that /Inovecky, 2003/ experienced exactly the same problems with a self-made finite element implementation of GIA. In his ANU benchmark test, testing against earth model 2 c /Kaufmann and Johnston, 1997/, he also ignored the fluid mantle, as we have here. We will pursue this matter further.
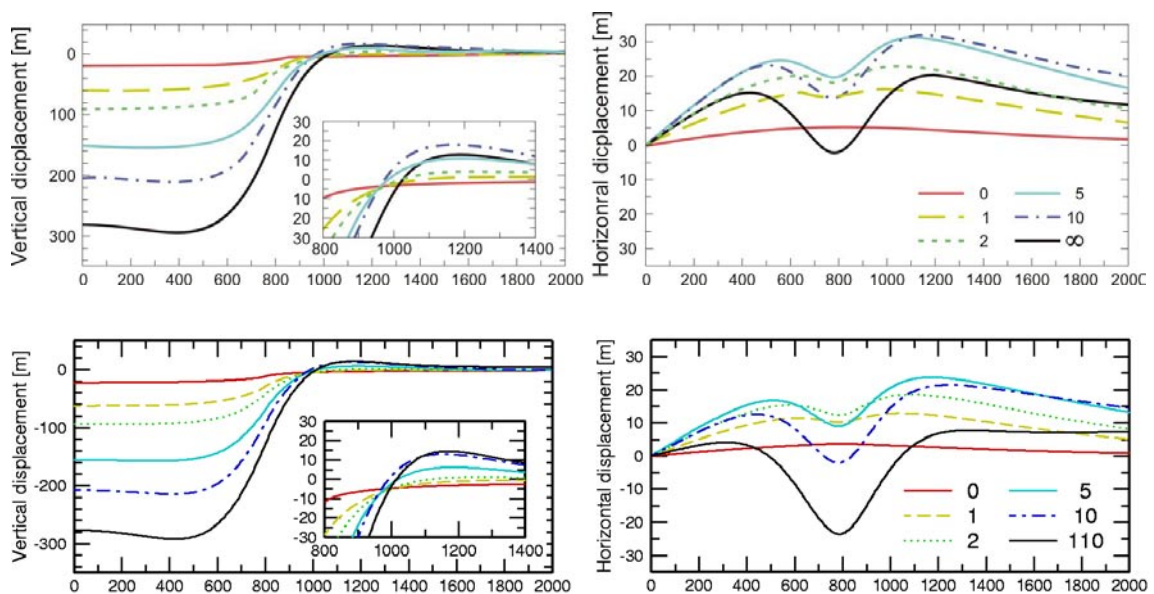

Figure 2-4. *Results of ANU benchmark test Earth 2a for GIA modelling /Kaufmann and Johnston, 1997/. Top: the ANU benchmark results for vertical displacements, left, and horizontal displacements, right. Bottom: Our results of the ANU benchmark test, vertical, left, and horizontal, right, displacements.*

2.3   Two dimensional reference model

In this report we will be testing the response of two dimensional earth models to glacial loading and unloading. As our reference model we will adopt the 2D version of the /Klemann and Wolf, 1998/ earth model, see Figure 2-2 and Table 2-1. We will also be using a 2D version of the elliptic ice model of /Klemann and Wolf, 1998/, with the linear time history described in section 2.2.2. All parameter variations presented below will be variations of this reference model. In Figure 2-5 we show the maximum horizontal and vertical stresses and in Figure 2-6 the maximum shear stress and stress state for the 2D model corresponding to the axisymmetric model above. Again, only the incremental rebound stresses are shown.

We see in Figure 2-5 the variations in horizontal stresses typical for these loading problems, with compressional horizontal stress under the load and tensional horizontal stress beyond the load margin at the surface. At depth in the elastic plate the situation is reversed, sometime after LGM, with tensional horizontal stress below the ice sheet and compression beyond. The vertical stress follow closely the ice load, but we note the viscoelastic relaxation of the mantle reloading the elastic plate from below. The principal stresses are horizontal and vertical in most of the model, but there is a region of increased shear stress central in the model, below the edge of the ice sheet, where the principal stress do not follow the horizontal and vertical. Figure 2-6 shows, as the axisymmetric Figure 2-2, the symmetry of the maximum shear stresses at LGM and the slow migration downward of the central, neutral surface as the rebound process progresses. Comparing to Figure 2-2, we note that the 2D implementation produces less shear stress under the ice at LGM than the axisymmetric model, but that outside the edge of the ice the shear stress is higher. The shape of the isolines has also changed. As seen in Figure 2-6, these differences remain throughout the deglaciation. We also note that the two-dimensionality of the model prohibits the existence of strike-slip stress states. The earth model used to produce Figure 2-6 was of equally high resolution as the axisymmetric model above. After the section on variation of element size, we will use a model with significantly fewer elements, and correspondingly faster computation times, as our 2D reference model.
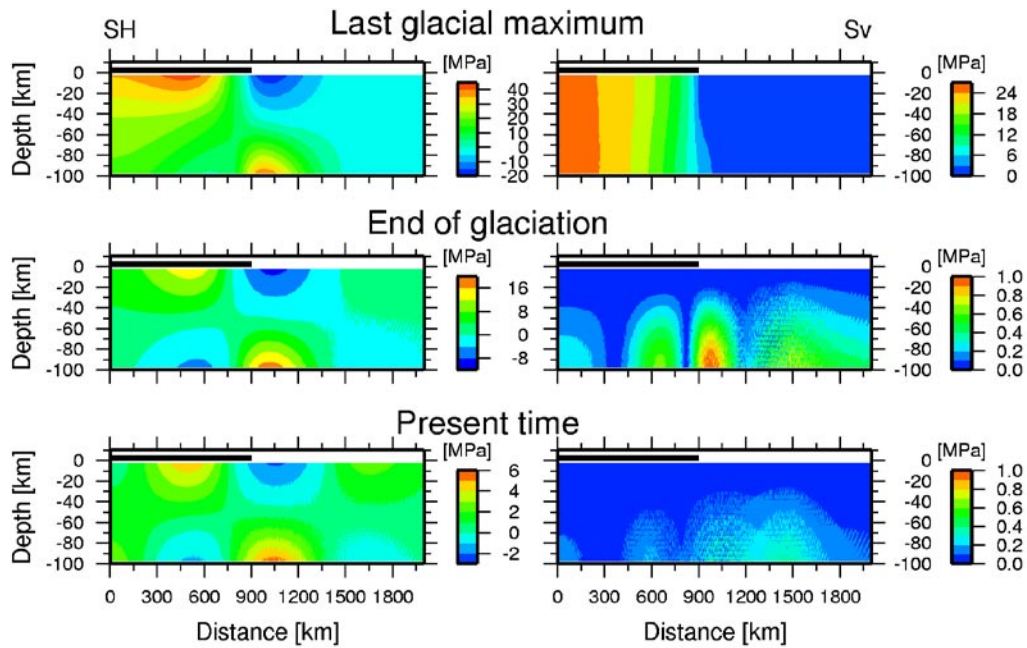
Figure 2-5. *Maximum horizontal (left) and vertical (right) incremental rebound stresses at three different times: LGM, end of glaciation and present.The model is the 2D reference model based on the /Klemann and Wolf, 1998/, axisymmetric earth and ice models.*
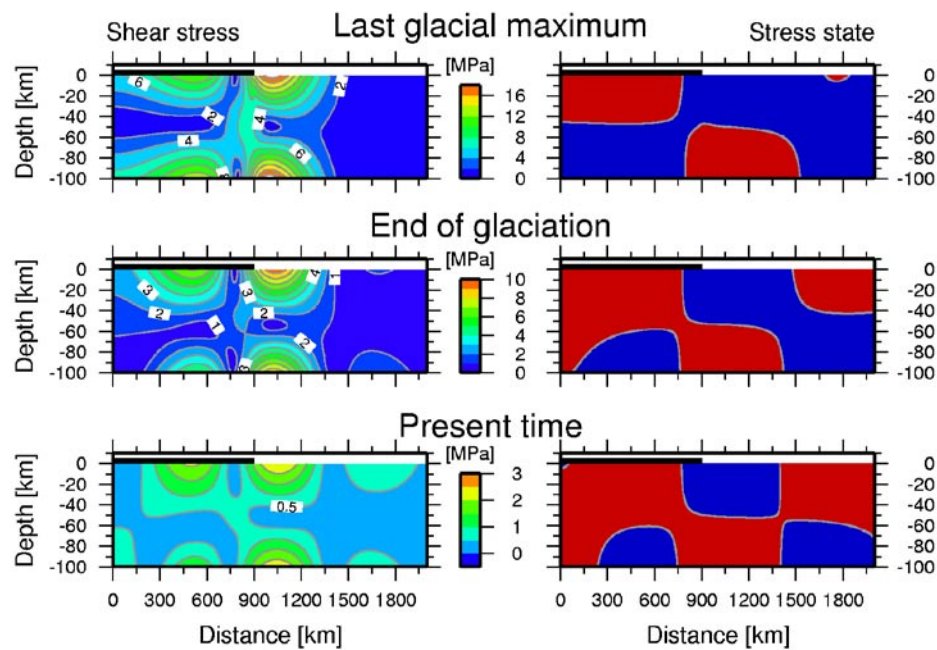
Figure 2-6. *Maximum shear stress and stress state response of the 2D two dimensional /Klemann and Wolf, 1998/ earth and ice models. All other features as in Figure 2-2.*

17

2.4   Summary

The validation of the finite element implementation, in the commercial Abaqus finite element analysis software, of glacial isostatic adjustment modelling has shown that the technique works well. The relative abundance of published result for axisymmetric models makes benchmarking axisymmetry easier than the 2D case, which is shown in the number of test cases above. Frequently, the presentations of results of GIA model are present as vertical surface displacement, or uplift rate. It is difficult to find good comparisons for the horizontal displacements and stress distributions, especially in two dimensions.

In the two dimensional case we find excellent agreement between our finite element model and the analytical expression for the vertical displacements due to a Heaviside load on a viscoelastic half-space. Our model also agrees very well with the 2D finite element models of /Wu, 1992/, both for Mises stress and vertical displacements of a viscoelastic half-space subject to a Heaviside load. /Wu, 1992/ also show results for the vertical displacements of a 2D model of an elastic plate on a viscoelastic half-space, subject to a Heaviside load, and our model agrees very well with that.

In order to validate the axisymmetric version of our finite element approach, we tested it using the viscoelastic half-space loaded by a Heaviside ice sheet of /Wu, 1993/. The results for vertical displacements agree very well with Wu's finite element model. Comparison with the results of /Klemann and Wolf, 1998/, who used the spectral technique to study an elastic plate overlying a viscoelastic half-space subject to an elliptical ice sheet, shows remarkably good agreement in maximum shear stress and stress state results. Finally, we tested one of the benchmark models, a radially variable , incompressible model having elastic properties derived from the PREM model /Dziewonski and Anderson, 1981/, of /Kaufmann and Johnston, 1997/. Our vertical displacements agree very well with the benchmark result, but the horizontal displacements decay significantly faster than those of the benchmark. We are currently investigating the cause of this discrepancy further, it may be due to the non-self-gravitating, flat-earth approximations.

As our reference model for the parameter variations discussed in the remaining sections of this report, we use a two dimensional implementation of the /Klemann and Wolf, 1998/ model discussed above. The earth model has a 100 km elastic plate overlying a viscoelastic mantle and the ice model is an elliptical cross-section ice with height varying linearly in time but constant covered area.

3 Element size and model extent

In this section we will explore how variations in the size of the finite elements, i.e. the density of the computational grid, and the overall size of the model affects the outcome of the computations. We will be using the two dimensional reference model discussed above, i.e. a 100 km thick elastic plate over a viscoelastic half-space. The reference model, ref3 in the figures below, has a basic element size of 1.5×0.5 km in the region 1,500×200 km, horizontally×vertically, and a total extent of 9,000×4,500 km. This extent is chosen as 10×5 times the ice sheet radius. The size of the elements is linearly increased in the horizontal direction from 1,500 km to 4,000 km by a factor of 1.01, and then from 4,000 km to 9,000 km by a factor of 1.5. Similarly in the vertical direction, the factor is 1.01 from 200 km to 900 km and then a factor of 1.5 from 900 km to 4,500 km. The model has a total of 721,731 elements and required 6 hours and 59 minutes of computing time. We have chosen to display shear stress and vertical displacement at the surface below since the shear stress relates directly to fault stability, and vertical displacement is a good observable. In the difference plots below we show the tested model minus the reference model.

3.1 Element size

We first study how increases in the basic element size in the horizontal and vertical directions, respectively, influence the near surface shear stress and the vertical displacement at the surface. Since the shear stress is evaluated at the centroid of each element, we picked a depth of 2.5 km for the shear stress comparisons. This is because our favoured vertical element size will be 5 km below. It implies, however, that the shear stress from other element sizes are acquired from different element rows, and sometimes by interpolation between two rows.

In Figure 3-1 we show the result of increasing the horizontal element size by a factor of four, i.e. the basic element size is now 6×0.5 km in model el40 which has 261,521 elements. We see that there is very little difference between the two models, both in shear stress and in displacement.

If we instead increase the vertical size of the basic elements with the same factor four, model el41 has 1.5×2 km elements, we see in Figure 3-2 that the shear stress is more sensitive to the vertical element size than the horizontal. The displacement response is more ambiguous. This model has 249,479 elements.

In order to reduce the number of elements significantly, we test a model with 12×5 km basic element size, el43 with 24,063 elements, in Figure 3-3. We see that the error in the shear stress is now becoming significant, specially for the shear stress distribution at present time. This is an unfortunate feature of all the element size tests, that the error in the shear stress distribution at present time is of the same size as the errors at LGM or EoG, although the absolute level of stress is significantly less. The error in vertical displacements is still very small.

We finally show a model, el30 in Figure 3-4, with basic element size 6×5 km but with a more rapid increase in element size outside of the core area. el30 has 27,666 elements, slightly more than el43, which gives an improvement in the shear stress components at EoG and at present time.
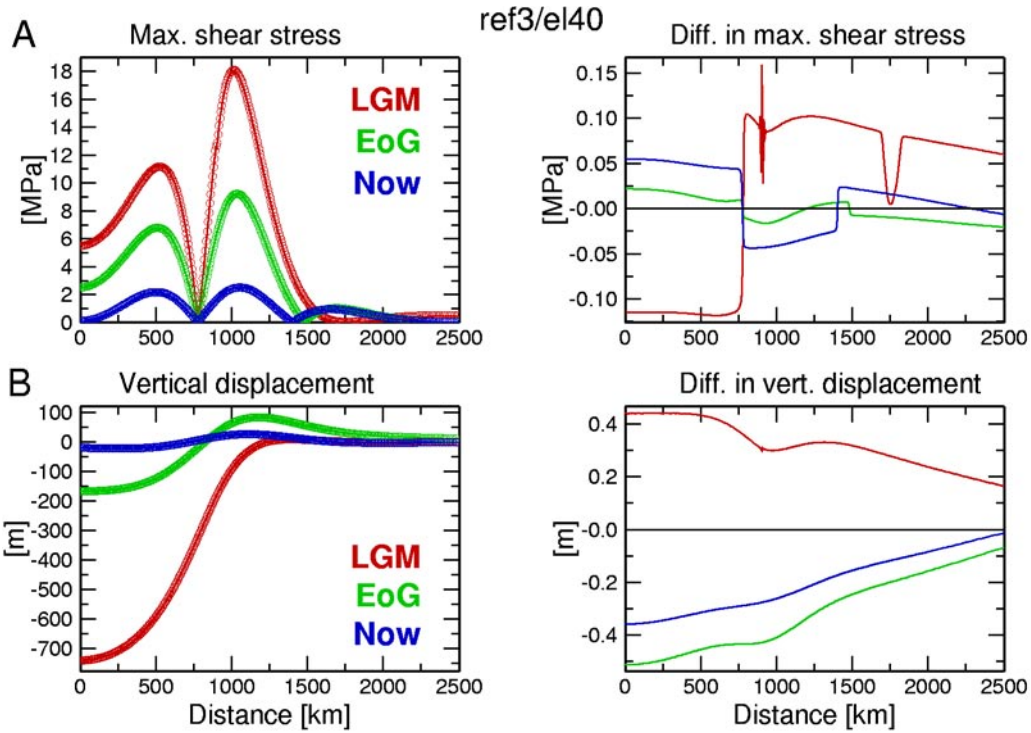
Figure 3-1. *A) Left: Maximum shear stress at 2.5 km depth along the first 2,500 km in the reference model ref3, solid lines, and in the test model el40, circles. Times are: LGM (red), end of glaciation (green) and present (blue). Test model el40 has 6×0.5 km large elements. Right: Difference between the shear stresses in model, el40, and the reference model. B) Vertical displacement at the surface in the reference model, solid lines, and the test model el40, circles, times as above. Right: Differences in the vertical displacements between el40 and ref3.*
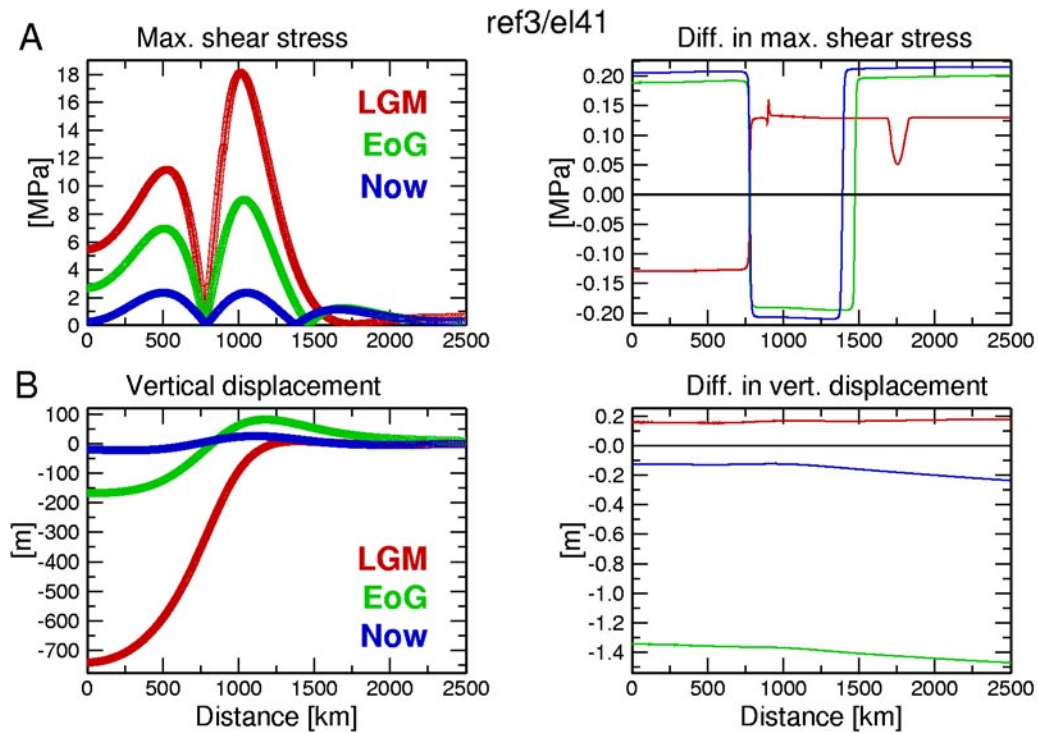
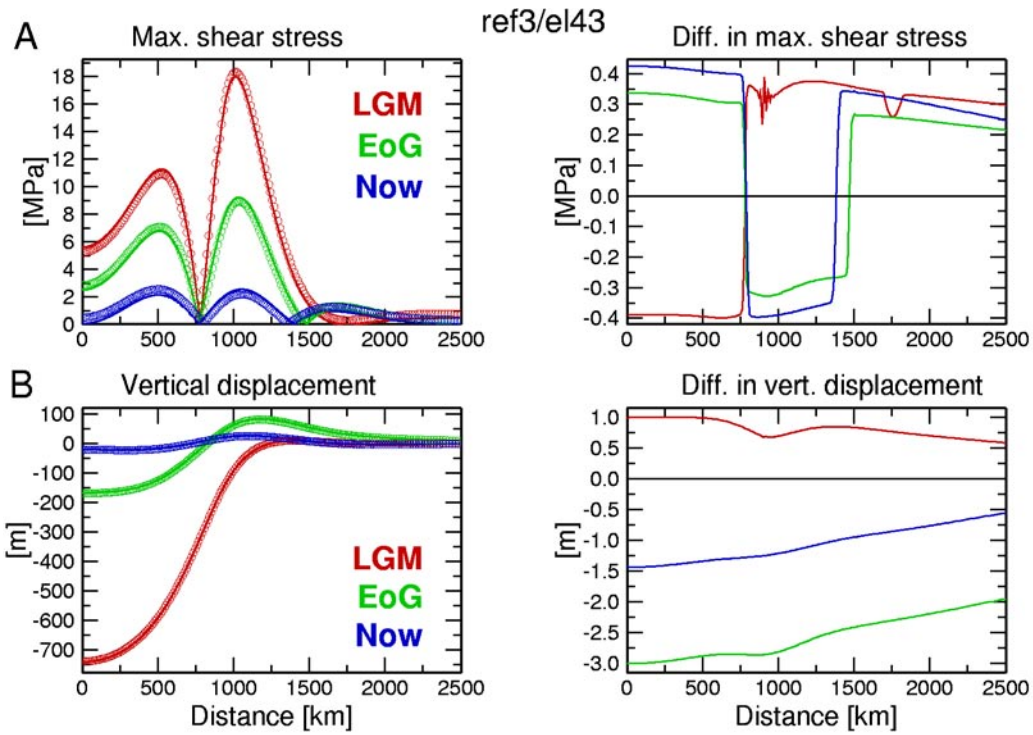**Figure 3-2.** *As Figure 3-1 but using test model el41, with 1.5×2 km elements.*

20

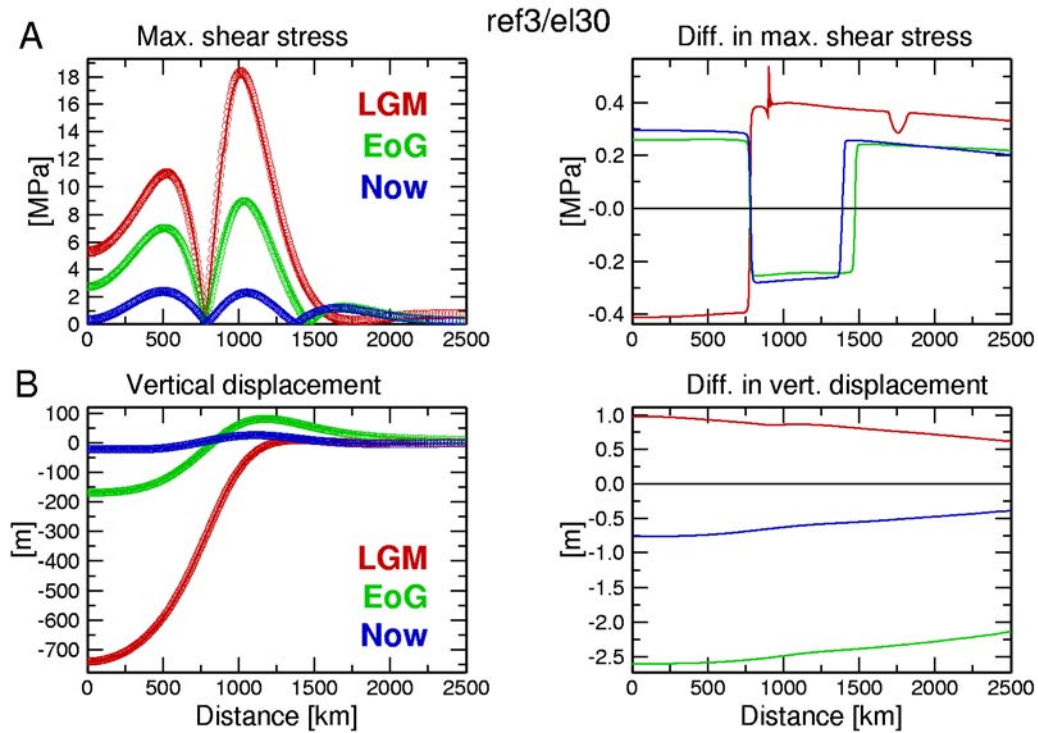**Figure 3-3.** *As Figure 3-1 but using test model el43, with 12×5 km elements.*

Figure 3-4 . *As Figure 3-1 but using test model el30, with 6×5 km element size.*

The run time for this model is 16 minutes, which is acceptable for this type of 2D study. We note, however, that going from 2D/axisymmetric models to 3D will require yet an increase in the element size. The model el30, with an element size of 6×5 km in the core area and a rapid increase in element size outside the core area, will be our reference model for the rest of this report.

3.2   Spatial extent of the model

Finite element analysis is sensitive to the spatial extent of the model, specially when use is made of infinite elements as model boundaries. Here we investigate how maximum shear stress and vertical displacements are affected as the model size changes. The reference model is now el30 from above, with the original 900 km radius ice sheet.

We first investigate the horizontal dimension of the model, using models with half, 4,500 km, and one fourth, 2,250 km, of the original size. Reducing the model length by 50% does not affect the results very much, we show instead the results from the 25% model, size2, in Figure 3-5.

Obviously, having the model end at 2.5 ice radii has a large effect on the results, specially at the edge of the model, but we see from Figure 3-5 that the effect on the displacements and the shear stress after deglaciation, up to approximately 1,500 km, is surprisingly small. Comparing to Figure 3-4 we also note that the effect of reducing the model length to some extent counteracts the effects of increasing the coarseness of the model on the EoG results. However, the model size reduction has a large effect on the shear stress at LGM , an effect which adds to the error from the increase in element size, Figure 3-4 and Figure 3-5. The 50% model similarly has largest errors in the LGM shear stress, increasing the effect of coarsening.
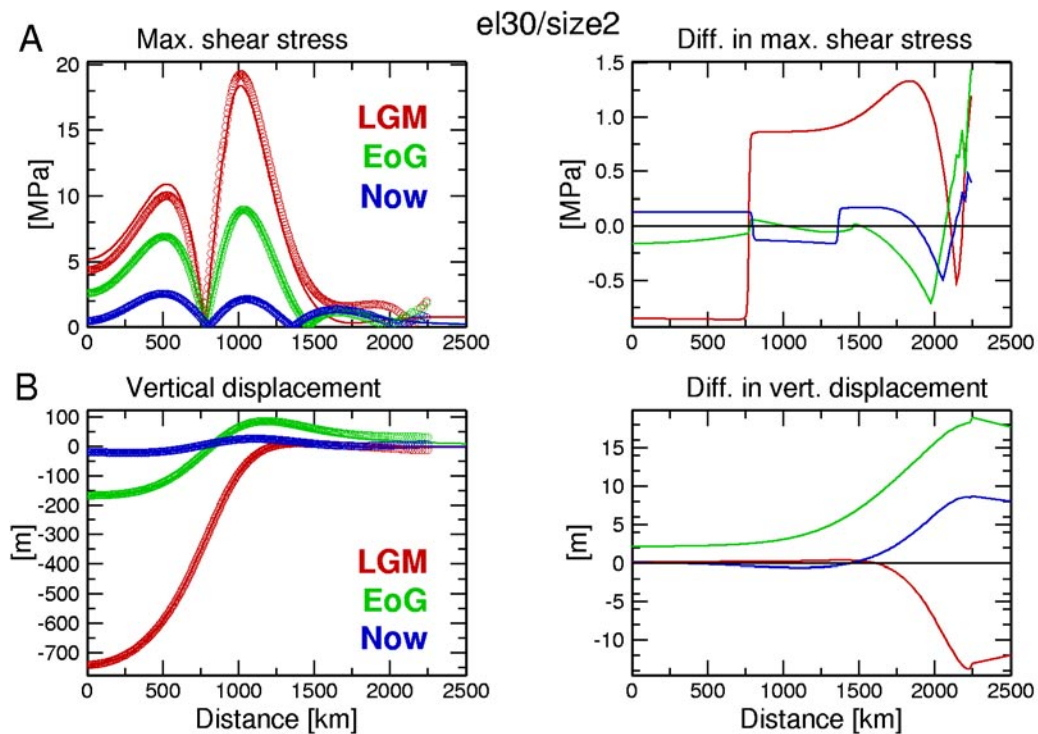
Figure 3-5. *Comparing the horizontal size of the model. Model size2 has 25% of the horizontal extent of model el30, i.e. 2,250 km. Lines and colours as in Figure 3-1.*
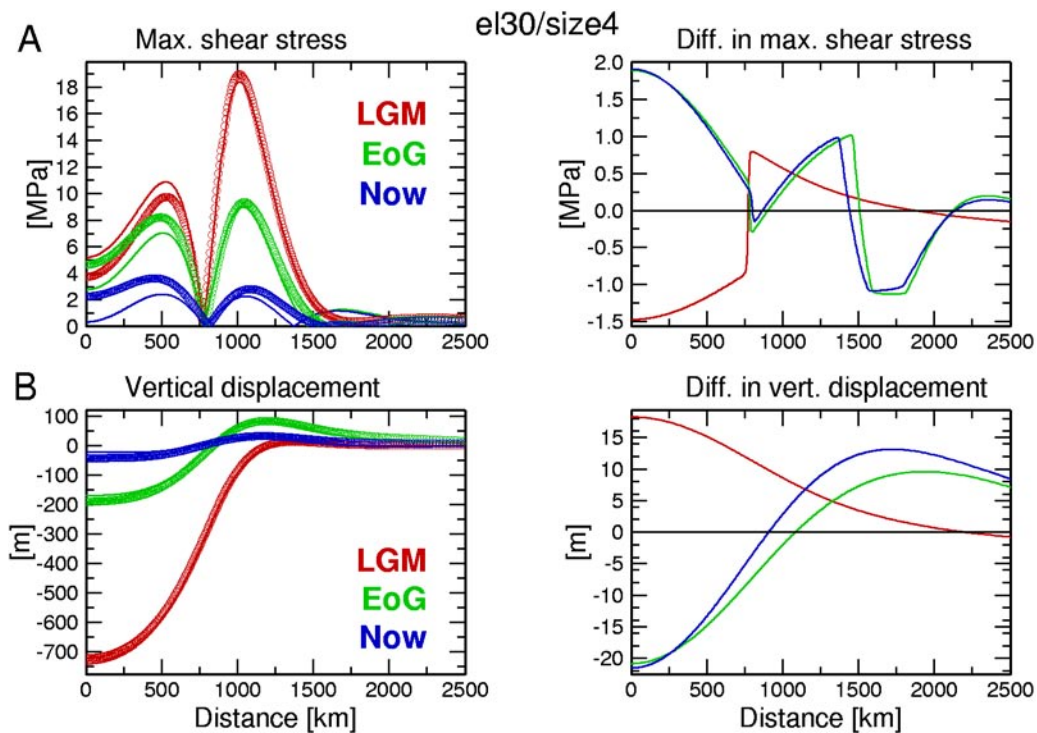
Varying instead the vertical size of the model, i.e. decreasing the depth, has a much larger impact on the results, as was indicated already in the element size study. We ran models with 50%, 25% and 12.5% of the reference depth of 4,500 km, and show the results for the 25%, 1,125 km deep, model size4 in Figure 3-6. Shear stresses and displacements, specially under the ice sheet, are now severely distorted and this model size is clearly unsatisfactory. The model with 50% of the reference depth also introduces errors in the results that are larger than what we can accept, larger in fact than the model size2 discussed above.

The models shown here, size2 and size4, have 22,994 and 24,634 elements, respectively, as compared to the 27,666 elements of the reference el30. The reduction in number of elements is clearly insufficient with respect to the large errors these models introduce.

We conclude by showing a model, size7, where we have increased both spatial dimensions to 20 by 10 ice radii, instead of the 10 by 5 of the reference el30, see Figure 3-7.

Comparing Figure 3-7 and Figure 3-4, we see that enlarging the model extent counteracts the errors in el30 compared to ref3, and significantly improves the model. Model size7 has 32,237 elements, 17% more than el30 and runs in 19 minutes instead of 16 minutes of el30. This difference is of no importance and if high resolution modelling is required, a large spatial extent is well spent computer resources.

Figure 3-6. *Comparing the vertical size of the model. Model size4 has 25% of the vertical extent of model el30, i.e. 1,125 km. Lines and colours as in Figure 3-1.*
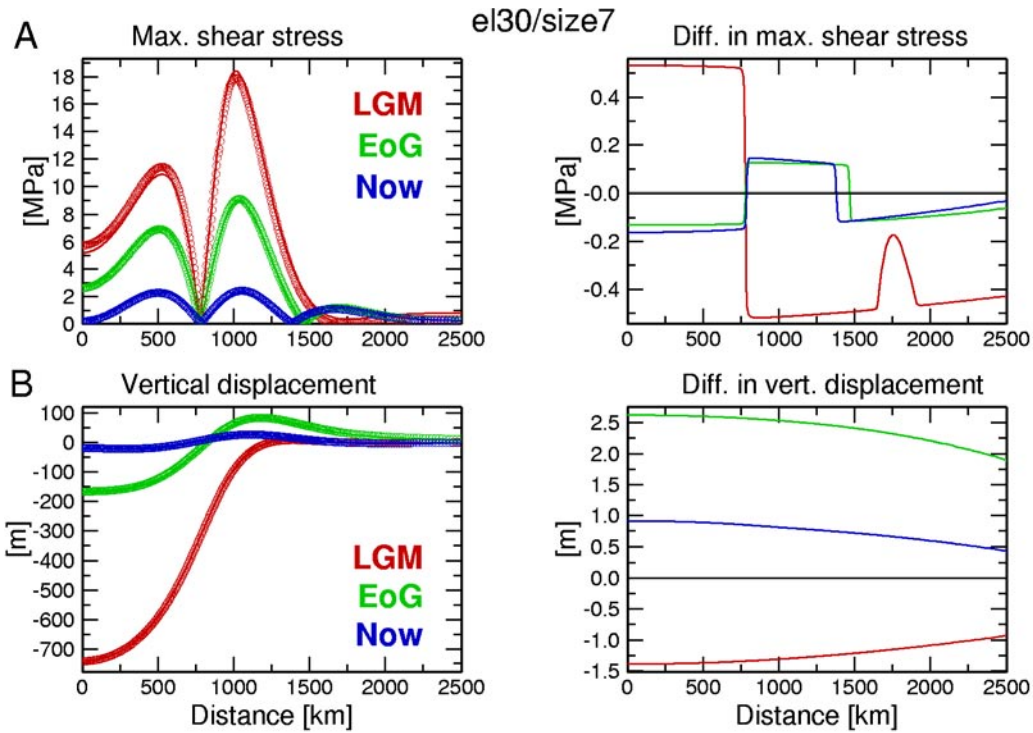
Figure 3-7. *Enlarging the model by a factor 2 in both dimensions, making it 20×10 ice radii.. Lines and colours as in Figure 3-1.*

3.3   Summary

The size of the finite elements can be increased significantly from the very high resolution used in the reference models without incurring large errors in the results. As shown above, the shear stress distribution is more sensitive to coarsening of the grid than the vertical displacement. We need also be aware that if high resolution studies of stresses close to the surface at present time is to be undertaken, these will require a dense grid. Increasing the element size from 1.5×0.5 km to 6×5 km, a factor of 40 in terms of square km, and coarsening the grid outside of the core area, still allows us to model the GIA process in sufficient detail. The modelling results are sensitive to changes in the total extent of the model, we have shown that 10×5 ice sheet radii is probably the smallest size advisable, and 20×10 should be used for high resolution studies.

4 Rheological parameters

This section is concerned with the rheological parameters of the Earth model, more specifically Young's modulus, viscosity, density, compressibility and the thickness of the elastic plate. These parameters can, obviously, be varied and combined in numerous ways. We shall limit this section to a few simple test cases in order to illustrate the effect the parameters have on the results of the modelling. As earlier, we shall restrict our attention to the output variables maximum shear stress, for its importance to fault stability, and vertical displacement, which is one of the primary observables. The performed variations and parameter values are listed in Table 4-1.

Table 4-1. Performed variations and corresponding parameter values. Empty cells indicate reference values and comma separated values refer to elastic plate and half-space, respectively.

| Case	Young's modulus [GPa]	Half-space viscosity [Pa s]	Density [kg/m^3]	Poisson's ratio	Elastic plate thickness [km]
Reference: el30	192, 435	1.0E+21	3,380, 3,380	0.5	100
Stiffness: par1	96, 435				
par2	384, 435				
par3	192, 217.5				
par4	192, 870				
Half-space viscosity par51		1.0E+20			
par6		1.0E+22			
Density par8			2,730, 3,380		
Material compressability compr1				0.25	
Elastic plate thickness lay1					20
lay2					50
lay3					150
lay4					200

4.1 Stiffness

The stiffness of different regions in the Earth is readily available from investigations of P- and S-wave velocities. The precise number to use, e.g. for Young's modulus, is, however, associated with some uncertainty, both due to the techniques used to measure and analyze the data, but also due to how the rock is modelled, e.g. including fluid effects or not. We vary Young's modulus in the elastic plate and in the underlying half-space separately in order to study the effect on our reference variables. Figure 4-1 shows the result of decreasing Young's modulus in the elastic plate by a factor of two, to 96 GPa in model par1, and in Figure 4-2 we increase the modulus by a factor of two, to 384 GPa in model par2.

We see, as expected, that by decreasing the stiffness, Figure 4-1, we obtain smaller stress magnitudes when the plate bends. We also note that the stress is more concentrated around the plate's inner inflection point. The opposite is true for the case of increased stiffness in Figure 4-2. The displacements show that the inner inflection point is not very much affected by the stiffness variations but that the outer inflection point moves outward, i.e. the fore-bulge is widened, as the stiffness is increased. We also note that decreased stiffness slightly increases the magnitude of the maximum displacement, and increases the height of the forebulge, whereas the opposite is true for increased stiffness.

Varying the stiffness in the viscoelastic half-space in the same manner, i.e. a factor of two decrease and increase, see Figure 4-3 where we only show the differences, we note that the half-space stiffness has a much smaller influence on the surface variables than the stiffness of the elastic plate.

Again, the effect of decreasing the stiffness is the opposite of the effect of increasing the stiffness, although now there is a slight offset in the "mirror" effect. This is perhaps an effect of the elastic plate.
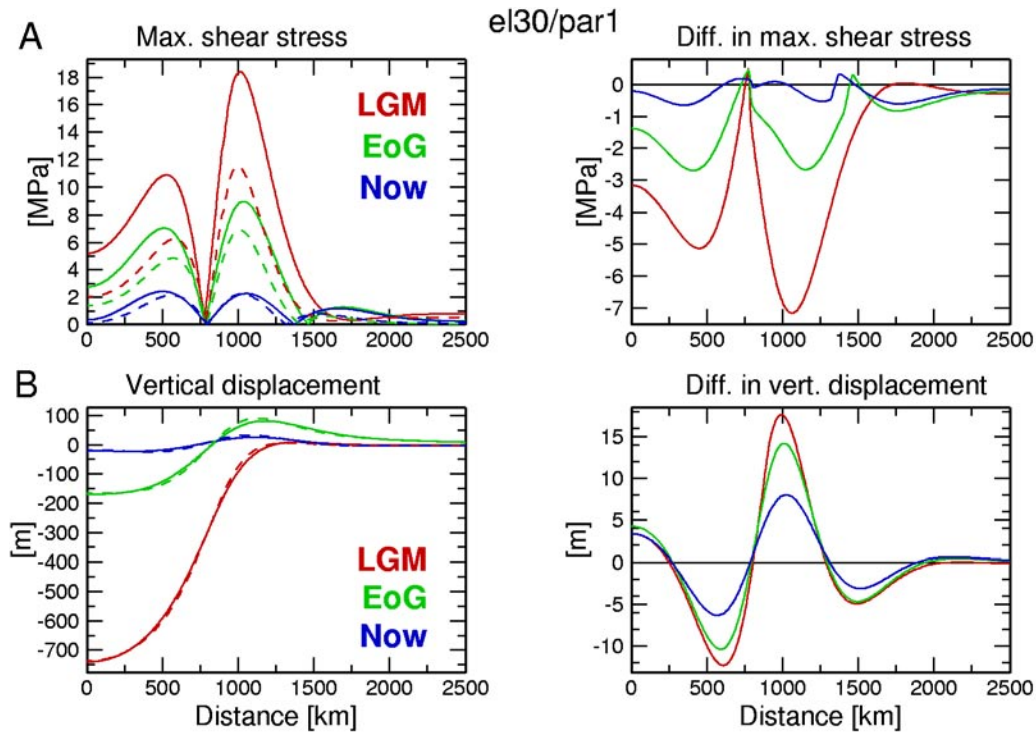
Figure *4-1. Young's modulus decreased by a factor 2, to 96 GPa, in the elastic plate. Solid lines are the reference model, dashed lines the test model par1. Colours as in Figure 3-1.*
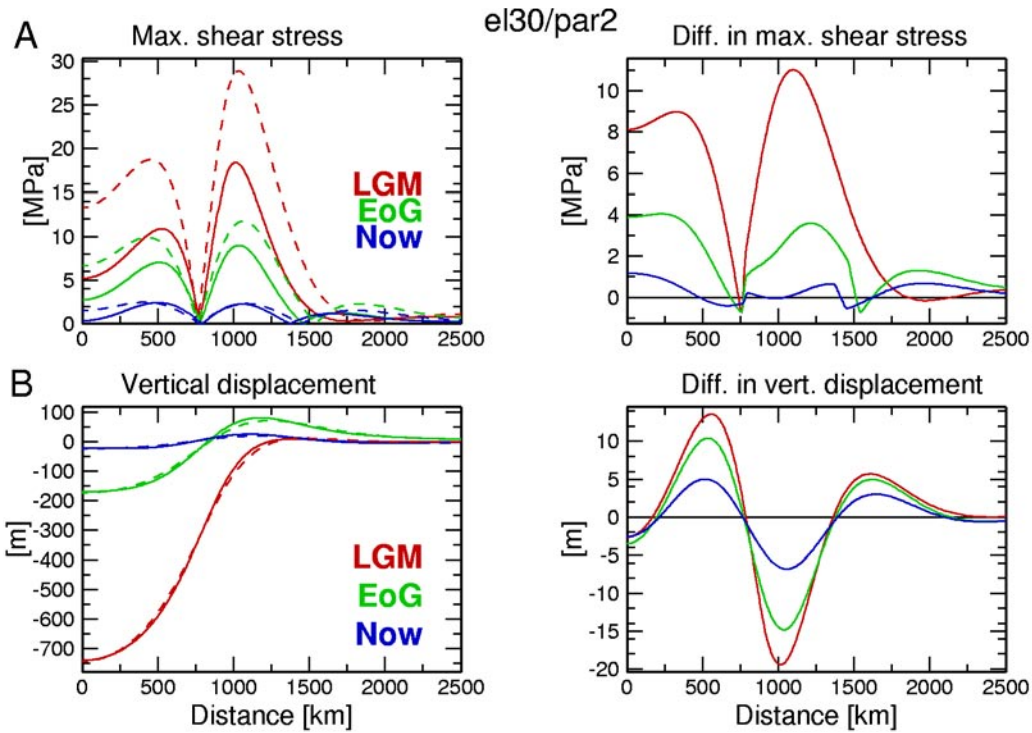
Figure 4-2. *Young's modulus increased by a factor 2, to 384 GPa, in the elastic plate. Lines and colours as in Figure 4-1.*
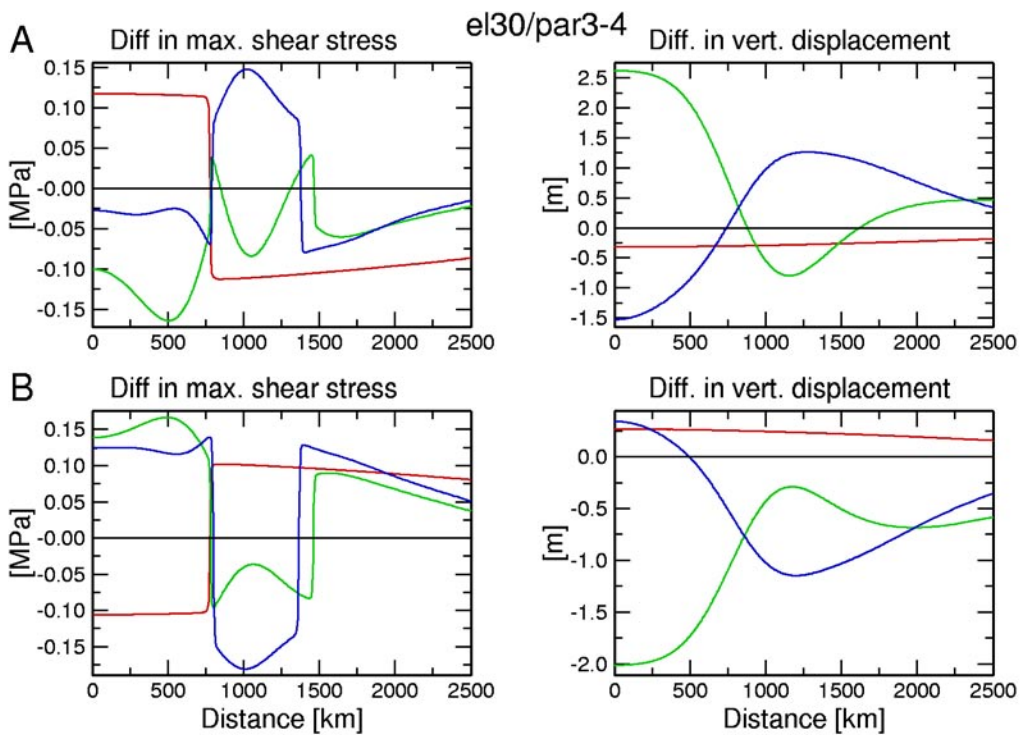

Figure 4-3. *A) Young's modulus decreased by a factor 2, to 217.5 GPa, in the half-space. Left: Difference in maximum shear stress. Right: Difference in vertical displacement. B) As in A, but with Young's modulus increased by a factor 2, to 870 GPa, in the half-space. Lines and colours as in Figure 3-1.*
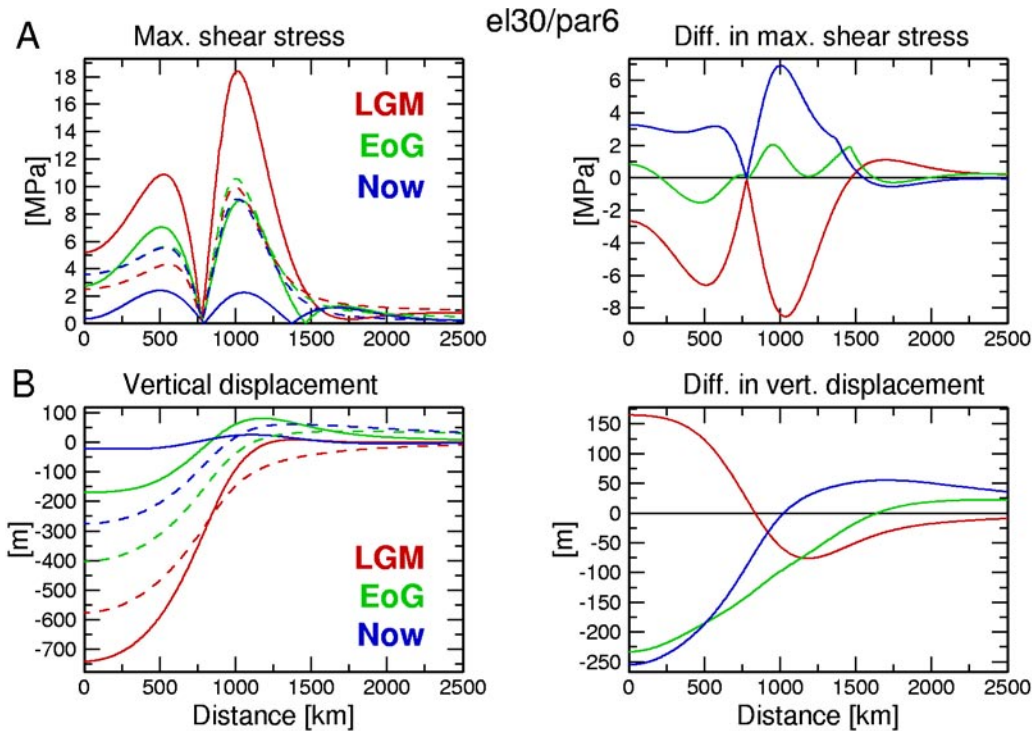
4.2 Viscosity of the half-space

The viscosity of the half-space determines the deformation rate of the GIA process and therefore both the stress and displacement distributions. Since our model is evaluated at specific times, without respect to the half-space relaxation time, the results for different viscosities will vary significantly, as shown below. We show results for model par51 in Figure 4-4, with viscosity 10^{20} Pas, and for model par6 in Figure 4-5, with viscosity 10^{22} Pas, compared to model el30 with viscosity 10^{21} Pas. Relaxation times are 49.5 years for model par51, 495 years for el30 and 4,951 years for par6.

Figure 4-4 shows how the low viscosity half-space responds quicker to the unloading of the ice sheet than the reference model, and has almost completed its rebound as the ice disappears at EoG. At LGM, there is less difference between the models, indicating that both models are close to the viscous limit. The high viscosity model in Figure 4-5, on the contrary, shows a slower response to the loading/unloading events, as expected. At LGM, model par6 has not deformed as much as model el30, the bending of the plate is much less, producing smaller shear stresses. Some of the difference between the vertical displacements at LGM and EoG is due to the elastic rebound as the ice is melted, we see that the bend in the overlying plate is very similar between the two times. The slow relaxation is striking at present time, where the high viscosity model has more then 250 m of residual rebound compared to the reference model.

These large effects of the viscosity on the vertical displacements are, of course, what makes glacial rebound studies such an excellent tool for inferences of mantle viscosity. We have not shown the horizontal displacements here, the effect on these are also large and provides additional constraints on viscosity structure, as discussed at length in e.g. /Milne et al. 2004/.
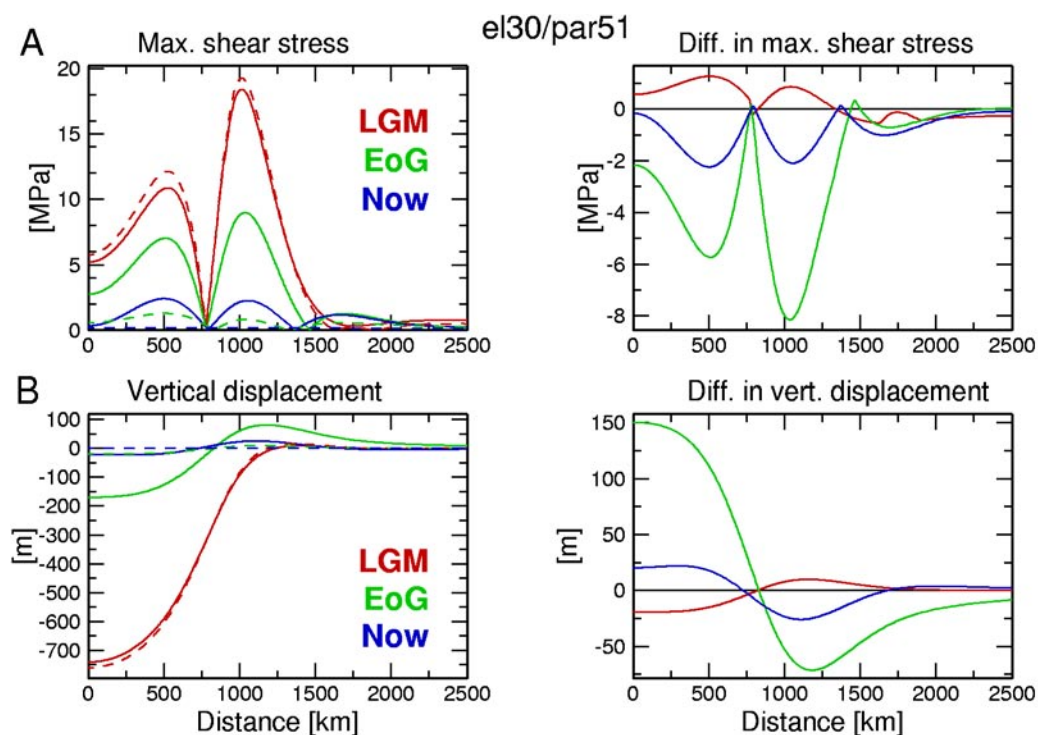
Figure 4-4. *Viscosity of the half-space decreased by a factor 10 to 10^{20} Pas. Lines and colours as in Figure 4-1*

Figure 4-5. *Viscosity of the half-space increased by a factor 10 to 10^22 Pas. Lines and colours as in Figure 4-1.*

4.3   Density

Estimates of Earth densities come from both velocity studies and gravimetry, and e.g. crustal models from large scale geophysical investigations frequently show high resolution in the density profiles. Incorporating density structure in GIA models is a longstanding topic of discussion /e.g. Wu and Peltier, 1982; Wu and Ni, 1996/, especially for models with density gradients, such as PREM /Dziewonski and Anderson, 1981/. Replacing density gradients with artificial density boundaries gives rise to extra buoyancy modes of relaxation, which may be undesirable. If, on the other hand, all density contrast is concentrated to an existing boundary, e.g. the Moho, then that boundary would have excessively large buoyancy forces. Different approaches to this problem exist in the literature, some use artificial boundaries, others average over a layer and concentrate the increase to an existing boundary and some studies use a "correct" density in the upper layer and then keep the density contrasts at the existing boundaries to the values obtained from the density models, resulting in lower than observed densities in all layers below the first.

Here we will only show a simple example of introducing density variations in the model. The elastic plate in model el30 has a density of 3,380 kg/m^3 and for model par8 we instead assign the plate a density of 2,730 kg/m^3. The underlying half-space retains the same density, 3,380 kg/m^3. Results are showed in Figure 4-6, and we see that the lower density plate produces considerably less shear stress under the load at LGM. There is very little effect on the vertical displacements. The "discontinuity" in the plot of difference in shear stress occurs at the inflection point, when we cross from a compressive regime under the load to a tensile regime, starting at approximately 750 km. This is where the horizontal stress increases above the vertical stress. The cause of the sudden decrease in horizontal stress for model par8, and how/if that is related to the difference in the buoyancy forces discussed above, is still being investigated.

29
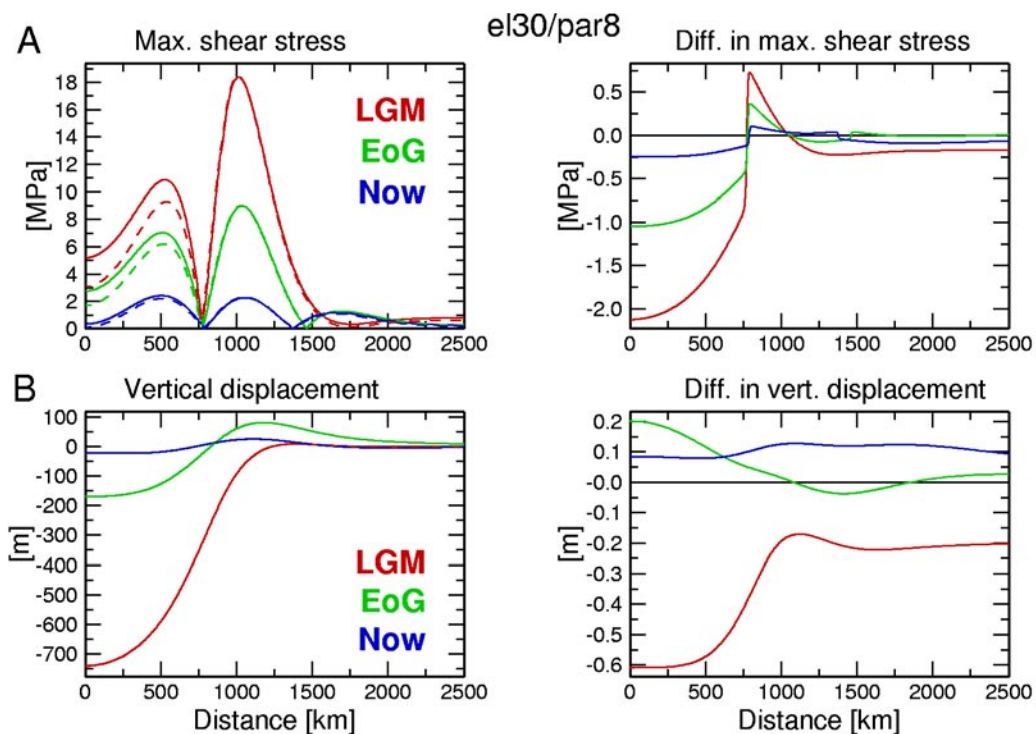
Figure 4-6. *Density in the elastic plate is reduced from 3,380 kg/m³ in model el30 to 2,730 kg/m³ in model par8. Lines and colours as in Figure 4-1.*

4.4   Material compressibility

Despite the fact that we, in the derivation of the simplified momentum equation above, explicitly had to refrain from including compressibility in our models in order for the finite element scheme to work, we can never the less incorporate material compressibility.

The third term in Eq 1 above, i.e. the buoyancy term $\rho^{\Delta} g_i^0$, can be artificially separated into two terms, one containing material compressibility, i.e. Poisson's ratio is less than 0.5 so that the bulk modulus is finite, and one containing internal buoyancy, i.e. the dilatation of material that causes buoyancy. This separation is not possible physically, having compressibility will cause dilatancy, but a number of authors have shown that it effectively removes instabilities associated with internal buoyancy while allowing for material compressibility, see review in /Klemann et al. 2003/. In terms of the finite element modelling, incorporating material compressibility is trivial since it is already an integral part of the software package.

In Figure 4-7 we show the result of including material compressibility in the model. The model compr1 has Poisson's ratio $\nu = 0.25$ in the entire model, a reasonable value for crustal rocks. We see that compressibility has a relatively large effect on the shear stress, specially at maximum load, which is generally decreased when the material can compress. The effect on the vertical displacements is smaller, we see, however, that the bend in the plate is slightly increased by compressibility. The overall effect of introducing material compressibility is, therefore, similar to a softening of the material, compare Figure 4-1 and Figure 4-7.

30
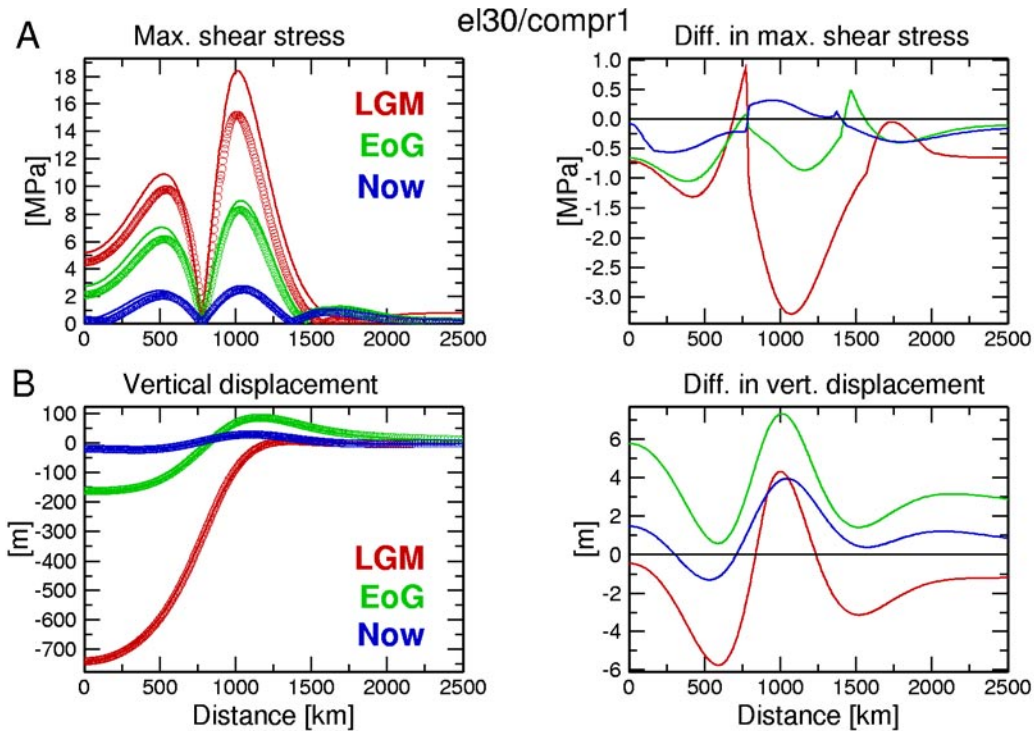
Figure 4-7. *Compressibility in the model. el30 is incompressible, compr1 has Poisson's ratio 0.25. Lines and colours as in Figure 3-1.*

4.5 Elastic plate thickness

Estimates of the thickness of the elastic lithosphere from GIA models range from approximately 50 km to 150 km /e.g. Milne et al. 2004; Lambeck et al. 1998a,1998b; review in Wolf, 1993/. We have studied how variations in the thickness of the elastic plate affects the shear stress and vertical displacements, using plate thicknesses of 20 km, 50 km, 150 km and 200 km. The results are presented in Figure 4-8 to Figure 4-10. The vertical displacements in Figure 4-8 and Figure 4-9 show, as expected, that the thinner plates have steeper ends and more pronounced forebulges than the thicker plates. Also, the inflection points move further away from the ice edge and there is less and less remaining rebound as the plate thickens. There is, however, very little difference in the maximum vertical displacements below the ice load center.

Turning to the maximum shear stresses in Figure 4-10, where we present the results for 50 km and 150 km elastic plates, we again see the effect of concentration of deformation at the ice edge for the thinner plate and the broadening of deformation for the thicker plate. At LGM, the thinner plate has higher stress levels outside and lower stresses inside the ice edge, than the reference model, and the thicker plate conversely higher stress levels below the plate and lower outside. At present time, the thinner plate has overall higher, and the thicker plate lower, shear stress magnitudes than the reference model.

Our results agree very well with those of /Klemann and Wolf, 1998/, who studied the same layer thicknesses using an axisymmetric model. The results here also conforms to general results for an elastic lithosphere on an inviscid/viscoelastic mantle, i.e. the effect of the lithosphere on stress and displacements increases with lithosphere thickness and the relaxation time decreases with increasing thickness. /Johnston et al. 1998/ showed that there is a critical wavelength of the load compared to the thickness of the elastic plate, which for

a spherical model with viscoelastic mantle was twice the load diameter equals 11.6 times the plate thickness. At the critical wavelength the glacially induced stresses are maximized. Our model has a critical wavelength of 4×900 km = 3,600 km and the corresponding plate thickness thus 310 km. Our results show increasing horizontal stresses under the ice load as the plate thickness is increased from 20 km to 200 km, in agreement with /Johnston et al. 1998/.
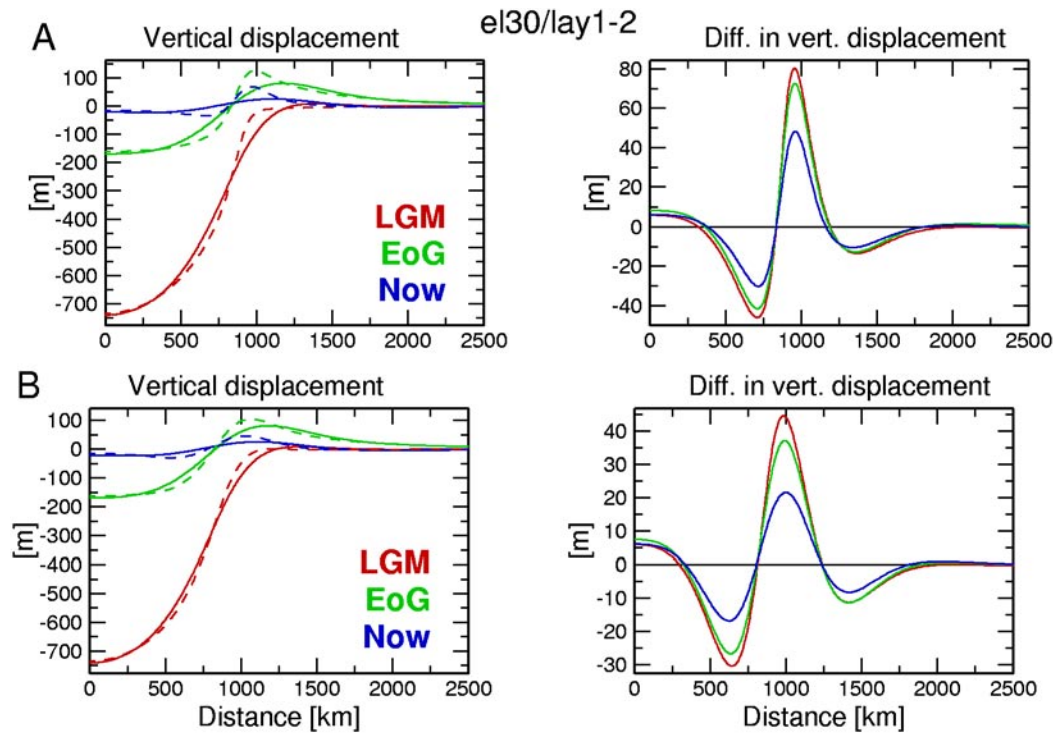
Figure 4-8. *A) Vertical displacements and displacement differences for the reference model and model lay1 with a 20 km thick elastic plate. B) Model lay2 with a 50 km thick elastic plate. Lines and colours as in Figure 4-1.*
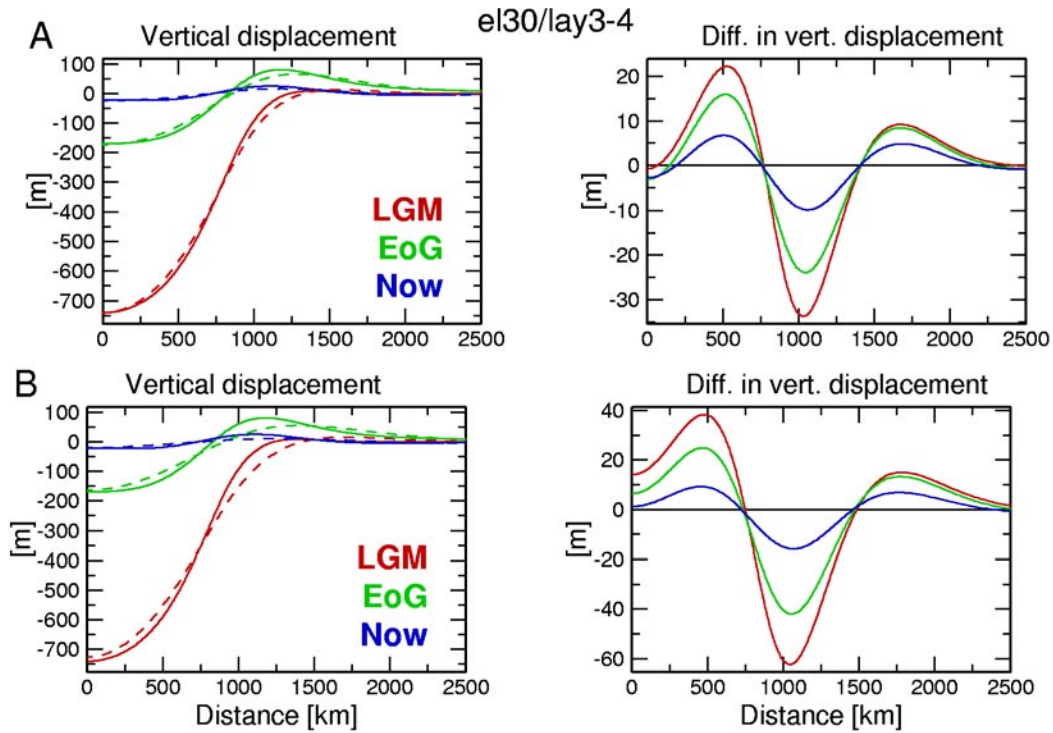
Figure 4-9. *A) Vertical displacements and displacement differences for the reference model and model lay3 with a 150 km thick elastic plate. B) Model lay4 with a 200 km thick elastic plate. Lines and colours as in Figure 4-1.*
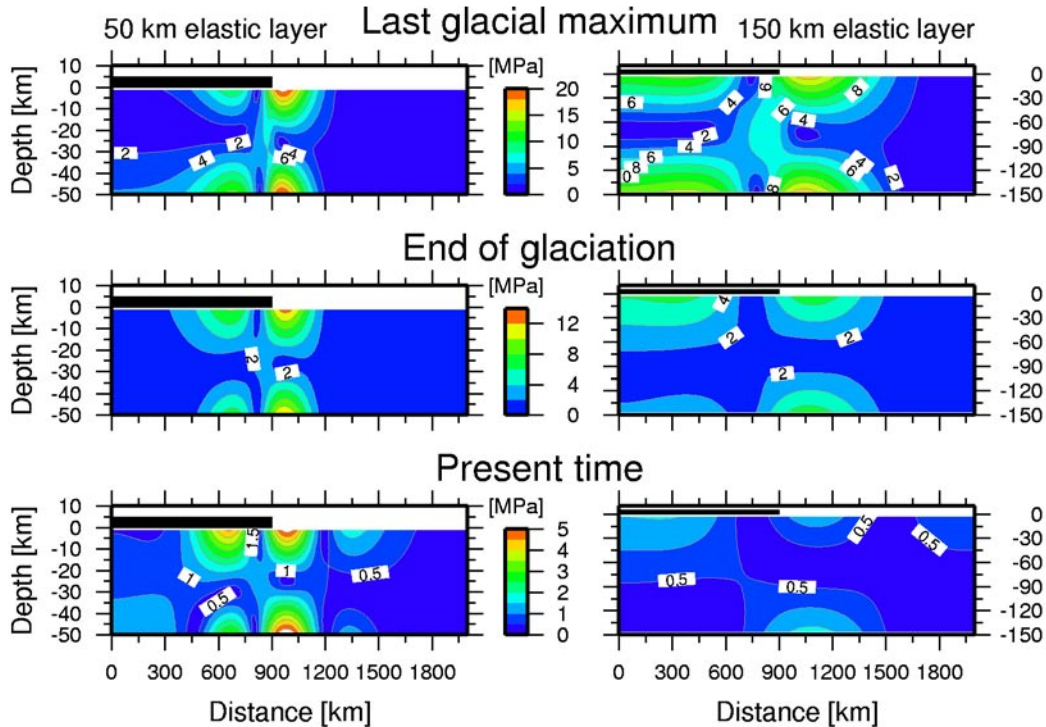
Figure 4-10. *Contour plots of maximum shear stress for the model lay2, left, with a 50 km thick elastic plate, and model lay3, right, with a 150 km thick elastic plate. Lateral distance from the center of the ice load versus depth. Three different times are shown, LGM at the top, end of glaciation in the middle and present time, bottom. The black bar on top of the plots indicate the extent of the ice at LGM.*

33

4.6 Summary

This section has studied the response of the reference earth model to variations in the rheological model parameters. Specifically, the effect on maximum shear stress and vertical displacement at the surface have been investigated.

- Varying the stiffness, represented by Young's modulus, of the elastic plate has a significant effect on the shear stress. Increased stiffness increases stress magnitudes and the size of the region of high stress, decreased stiffness conversely decreases stress magnitudes and the high stress region size. The stiffness has less effect on the vertical displacements.

- Stiffness variations in the viscoelastic half-space has almost no effect on the surface variables.

- The viscosity of the half-space governs the temporal evolution of the model and, therefore, evaluating the model response at specific times will show large variations in both shear stress and vertical displacement with viscosity. Low viscosity implies fast response to variations in the load and, thus, small deglaciation stresses and displacements, whereas the opposite is true for a high viscosity half-space.

- Density variations need to be carefully implemented in the model not to produce unwanted buoyancy effects and mainly affect the region of the model under the load, which has the largest vertical displacements. Lowering the density of the elastic plate produces less shear stress under the load, but does not significantly affect the vertical displacements.

- Introducing material compressibility into the model produces an effect similar to a softening of the material.

- The thickness of the elastic plate has a large effect on the distribution and magnitude of both shear stress and vertical displacement. For a thinner plate, the bending at the ice edge increases and, consequently, shear stress localizes at the ice edge with relatively high magnitudes. Conversely, a thicker elastic plate produces less bending, more evenly distributed shear stress with lower magnitude at the ice edge and higher shear stress at the center of the load.

These model parameter variations show that, in general, the maximum shear stress is more sensitive to parameter changes than is the vertical displacements. This is a little unfortunate, as vertical displacement is one of the very few observables readily available to us in studying glacial isostatic adjustment. The modelling result show that it can be very difficult to discern which model parameter is responsible for a change in the model response, as an increase in e.g. compressibility can be obscured by a decrease in stiffness. However, the results of this section are very useful to understand the contributions of the various parameters to the GIA response.

5   Multiple layers on a half-space

In this section we investigate the implications of dividing the elastic plate into an upper, elastic layer and a lower ductile layer. This is not primarily an effort to model a more realistic lithosphere, as that would probably be better modelled by a three-layer structure with a lower viscosity middle layer, but rather a visualization of the effects of a second, ductile layer.

The models shown in Figure 5-1 and Figure 5-2 have a 50 km elastic plate on a 50 km viscoelastic layer, overlying a viscoelastic half-space, with model mlay5 having viscosity 10^{20} Pa.s and model mlay1 10^{22} Pa.s. All other parameters are as for the reference model, e.g. Young's modulus is 192 GPa down to 100 km. The vertical displacements in Figure 5-1 behave as expected, the replacement of the lower 50 km of the reference plate with a ductile material thins the plate, c.f. Figure 4-8, and thus makes the plate bend more and accentuates the forebulge.
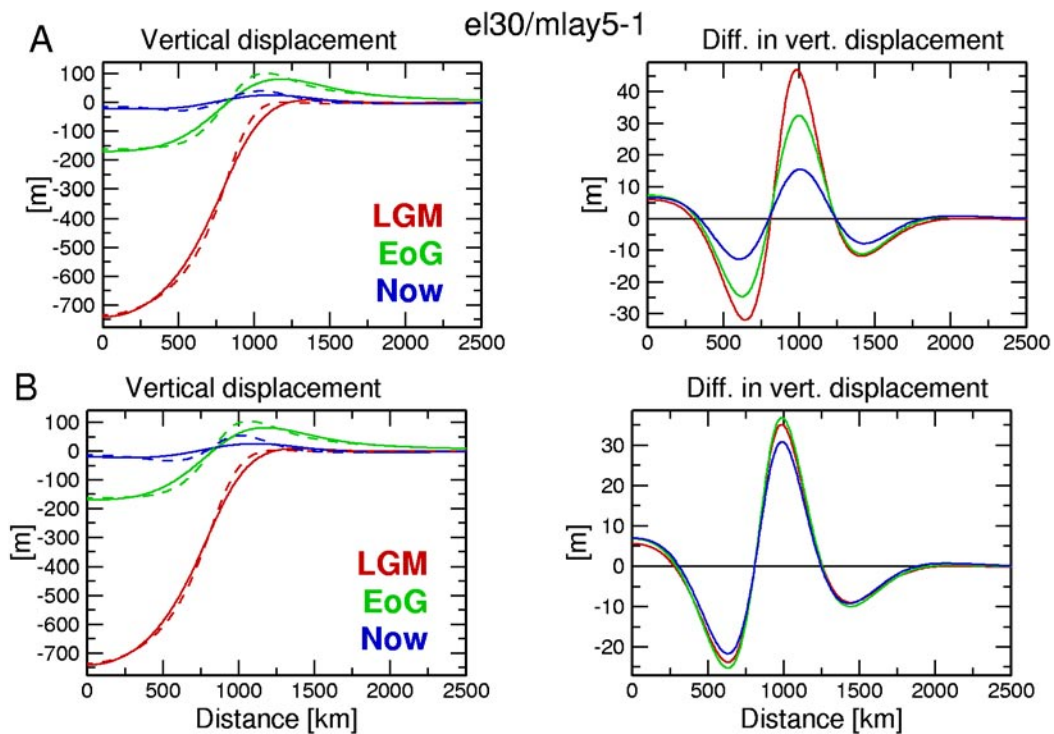
Figure 5-1. *A) Vertical displacements and displacement differences for the reference model and model mlay5 with a 50 km thick elastic plate overlying a 50 km thick viscoelastic plate with viscosity 10^20. B) Model mlay1 with a 50 km thick elastic plate overlying a 50 km thick viscoelastic plate with viscosity 10^22. Lines and colours as in Figure 4-1.*
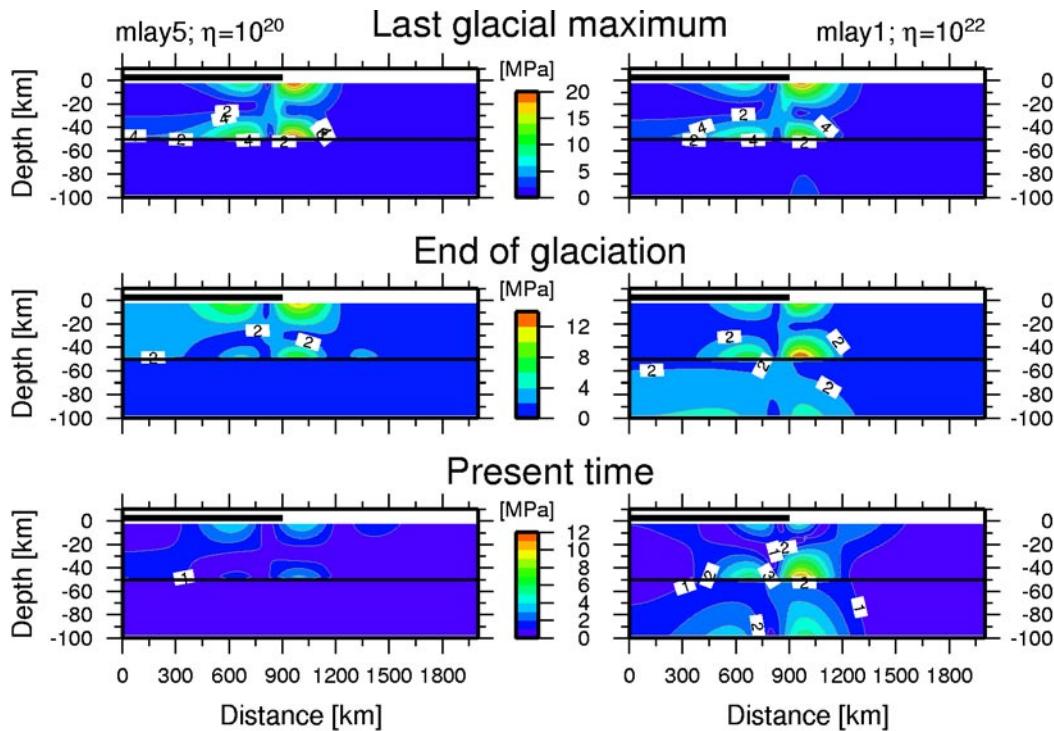
Figure 5-2. *Contour plots of maximum shear stress for the model mlay5, left, with a 50 km thick elastic plate overlying a 50 km thick viscoelastic plate with viscosity 10^20, and model mlay1, right, with a 50 km thick elastic plate overlying a 50 km thick viscoelastic plate with viscosity 10^22. Lateral distance from the center of the ice load versus depth. Three different times are shown, LGM at the top, end of glaciation in the middle and present time, bottom. The black bar on top of the plots indicate the extent of the ice at LGM.*

The shear stress distributions in Figure 5-2 show how stress is relaxed differently in the two models. The short relaxation time of the ductile layer in mlay5 instantly relaxes stresses in the second layer and there is very little stress transfer between the upper plate and the half-space. Conversely, the higher viscosity layer in model mlay1is slower to relax shear stresses and stress is transferred to and from the half-space.

The shear stress distribution in the upper plate for the mlay1 model is similar to the distribution for the model with only a 50 km thick elastic plate on the half-space, model lay2 in Figure 4-10, except for the larger magnitudes as present time for mlay1. This is a result of the stress transfer from below. Model mlay5, however, is very different to model lay2 due to the quick stress relaxation.

6 Lateral heterogeneity

The introduction of lateral heterogeneities in Earth models evaluated by spectral GIA techniques is rather difficult and, therefore, finite element analysis is generally used instead. There has until recently been very few studies published on the effects of lateral variations on the results of GIA modelling, notable exceptions being the early studies by Sabadini and coworkers /e.g. Sabadini et al. 1986; Gasperini and Sabadini, 1989/ and later by Kaufmann and Wu and coworkers /e.g. Kaufmann et al. 1997; Kaufmann and Wu, 2002/.

Here we show three simple examples of the introduction of lateral variations in the reference model. The 100 km thick elastic plate of the reference model is abruptly thinned to 50 km in the models below. In model lat1 the thinning occurs halfway between the center of the ice and the edge, i.e. at 450 km. In model lat2 the thinning is at the ice edge, at 900 km, and in model lat3 the discontinuity is at 1,350 km, i.e. 1.5 ice radii. The material properties of the thinned plate are everywhere identical to the plate of the reference model, and the underlying half-space properties are used for the infill where the plate has thinned. These models simulate the thinning of the lithosphere at a plate margin, such as off the coast of Norway.

Studying first the vertical displacements, we see in Figure 6-1B to Figure 6-3B that when only the central section of the plate is 100 km thick the displacements are more similar to the displacements of a 50 km thick plate, c.f. Figure 4-8B, than a 100 km thick plate. As the discontinuity in plate thickness moves further away from the center of the load, the displacements grow more similar to the reference model. These results agree very well with a similar study in /Kaufmann et al. 1997/, who show results for vertical displacements and land uplift.

The lateral heterogeneity has a much more profound influence on the shear stress. We see in Figure 6-1A and Figure 6-3A that there are a "kinks" in the shear stress distributions at the location of the discontinuity. For model lat1, shear stress under the ice is rapidly varying, and the shear stress diminishes quicker away from the ice edge compared to the reference model. As the thickness discontinuity moves away from the ice center, the shear stress distributions become more similar to the reference model, although there are variations in the locations of the inflections points, model lat2, and the kink in model lat3.

We conclude that lateral variations in the Earth model may have significant impact on the stability of faults, depending on their spatial distribution with respect to the material discontinuities.
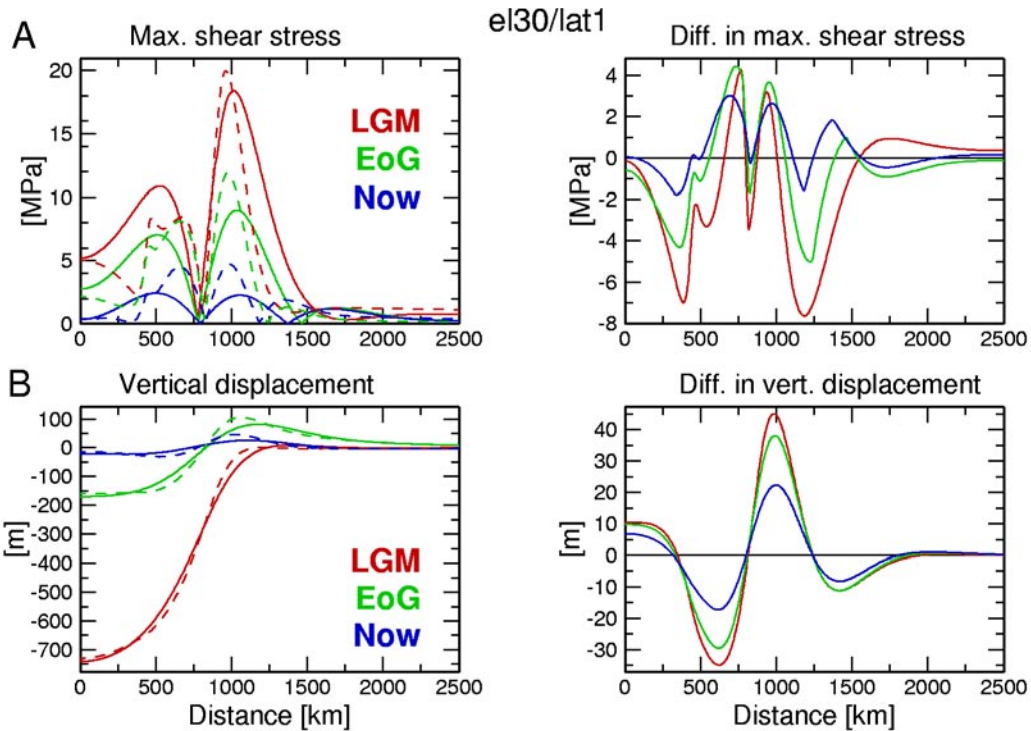
Figure 6-1. *Maximum shear stress and vertical displacement, and differences, for the reference model and model lat1, which has a 100 km thick elastic plate to 450 km laterally, and then a 50 km thick elastic plate. Lines and colours as in Figure 4-1.*
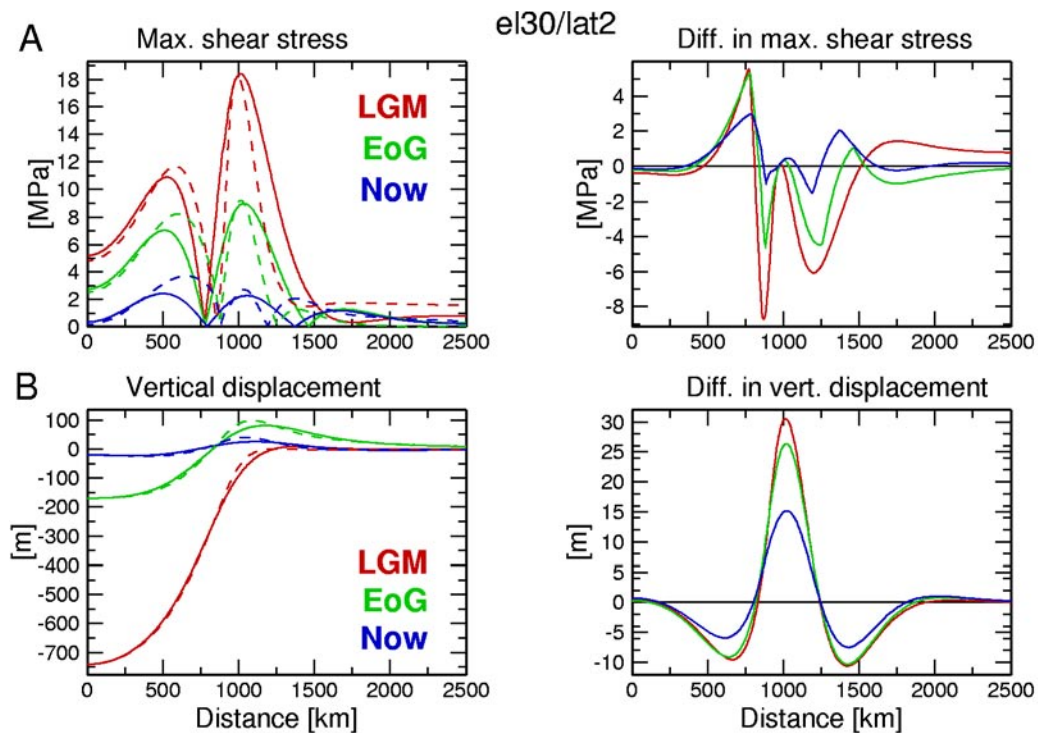
Figure 6-2. *Maximum shear stress and vertical displacement, and differences, for the reference model and model lat2, which has a 100 km thick elastick plate to 900 km laterally, and then a 50 km thick elastic plate. Lines and colours as in Figure 4-1.*
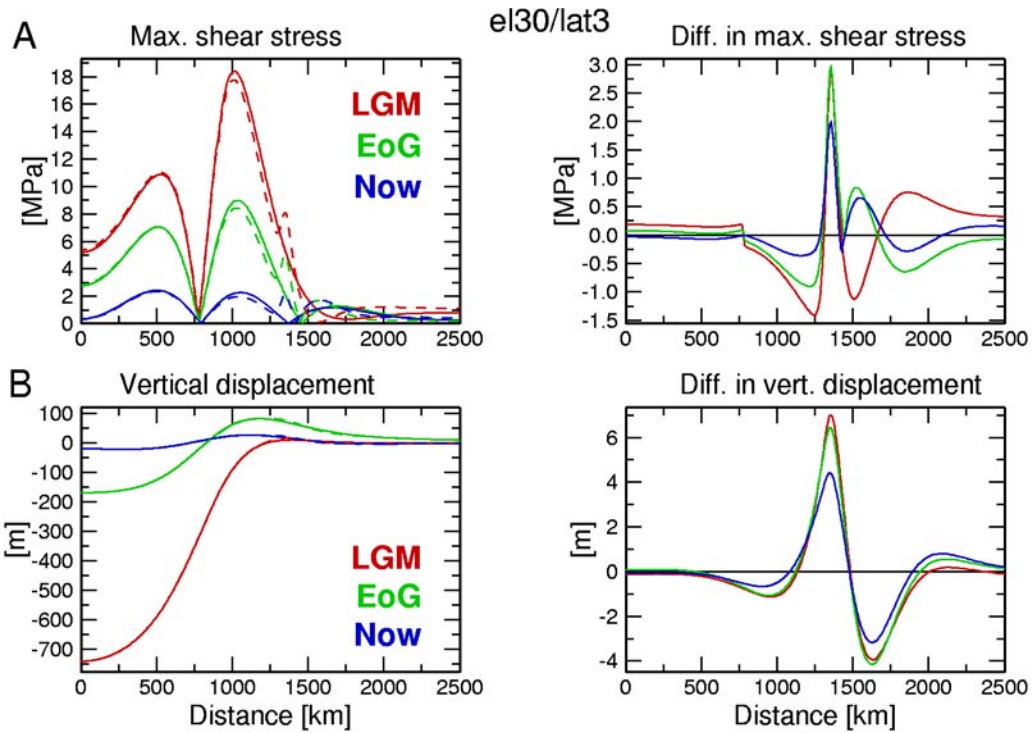
Figure 6-3. *Maximum shear stress and vertical displacement, and differences, for the reference model and model lat3, which has a 100 km thick elastick plate to 1,350 km laterally, and then a 50 km thick elastic plate. Lines and colours as in Figure 4-1.*

7 Ice models

The ice model is of paramount importance for the response of any Earth model. In this section we investigate how various ice models change the Earth response, using our usual variables of shear stress and vertical displacement. The reference model has been using an elliptical cross-section ice model, with lateral extent 900 km from center to edge, and a central height of approximately 2.8 km to produce a central load of 25 MPa. The ice has been stationary at 0–900 km, only the height of the ice has varied as the ice grows and shrinks. Below we will study ice models with a parabolic and a rectangular cross-section, and also a non-stationary elliptic ice model.

7.1 Stationary ice models

Here we will study the response of parabolic and rectangular ice sheets which occupy the same area during the modelling and only change their height, as with the reference ice model. Apart from the cross-sections, the ice models will be using the same parameters as the elliptic reference ice. Ice volumes, or rather areas as we model in 2D, in the three cases are related as $1:\pi/4:2/3$ for the rectangular, elliptic and parabolic cases, respectively. The rectangular ice has a pressure discontinuity of 25 MPa at the ice margin, whereas the elliptic and parabolic ice sheets decrease continuously toward the margin. The elliptic ice has an infinite pressure gradient at the margin, where the parabolic ice, conversely, has a finite gradient.

The vertical displacements in Figure 7-1 show, as expected, that the ice sheets produce approximately the same vertical displacement under the center of the ice, but that the parabolic ice produces less bending and the rectangular ice more bending than the reference elliptical ice.

Shear stress distributions in Figure 7-2 show that the location of the inner maximum, under the ice sheet, is localized close to the ice edge for the rectangular ice and is much broader, with the maximum at the center of the load, for the parabolic ice. This is in agreement with the variation in bending observed in Figure 7-1. Comparing with Figure 2-6, we see that the response to an elliptic ice is an intermediate between the rectangular and parabolic ice sheet responses. The shear stress maxima of the rectangular ice at LGM are of the same magnitude as the load pressure, whereas the maxima of the elliptic and parabolic ice sheets are smaller. The large differences in the locations of the inner maxima are not reflected in the outer maxima, the rectangular ice outer maximum is slightly further away from the ice margin than those of the elliptic and parabolic ice sheets, but the difference is small. There is a unique area of high shear stress located at mid-depth below the ice margin in the rectangular ice sheet model at LGM. Here the shear stress is of similar magnitude as the other stresses, causing a region of very unstable stress state.
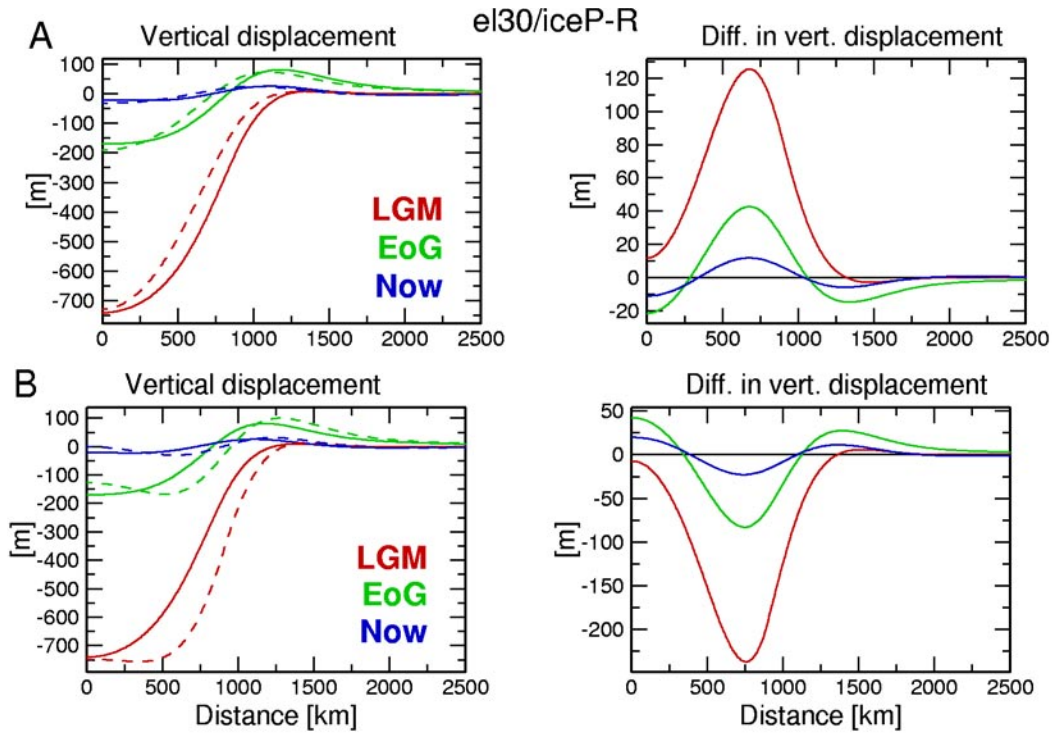
Figure 7-1. *A) Vertical displacement, and differences, of the reference model and model P with a parabolic cross-section ice load. B) Vertical displacements and differences of the reference model and model R with a rectangular cross-section ice load. Lines and colours as in Figure 4-1.*
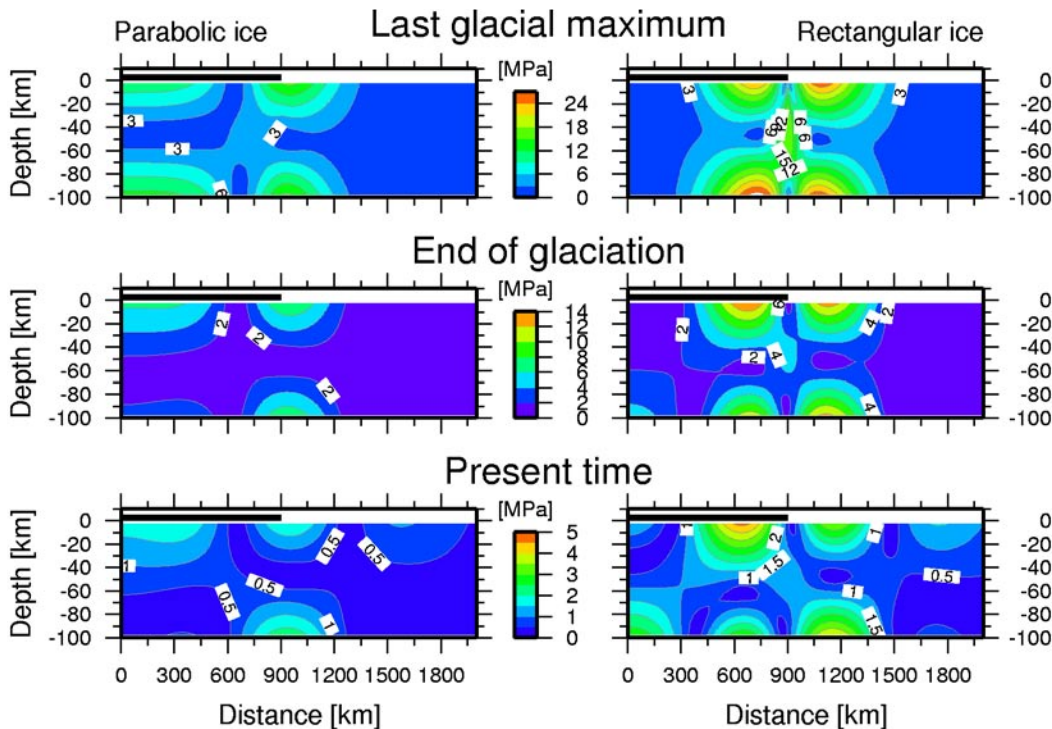
***Figure 7-2.*** *Contour plots of maximum shear stress for the model P, left, with a parabolic cross-section ice load, and model R, right, with a rectangular cross-section ice load. Lateral distance from the center of the ice load versus depth. Three different times are shown, LGM at the top, end of glaciation in the middle and present time, bottom. The black bar on top of the plots indicate the extent of the ice at LGM.*
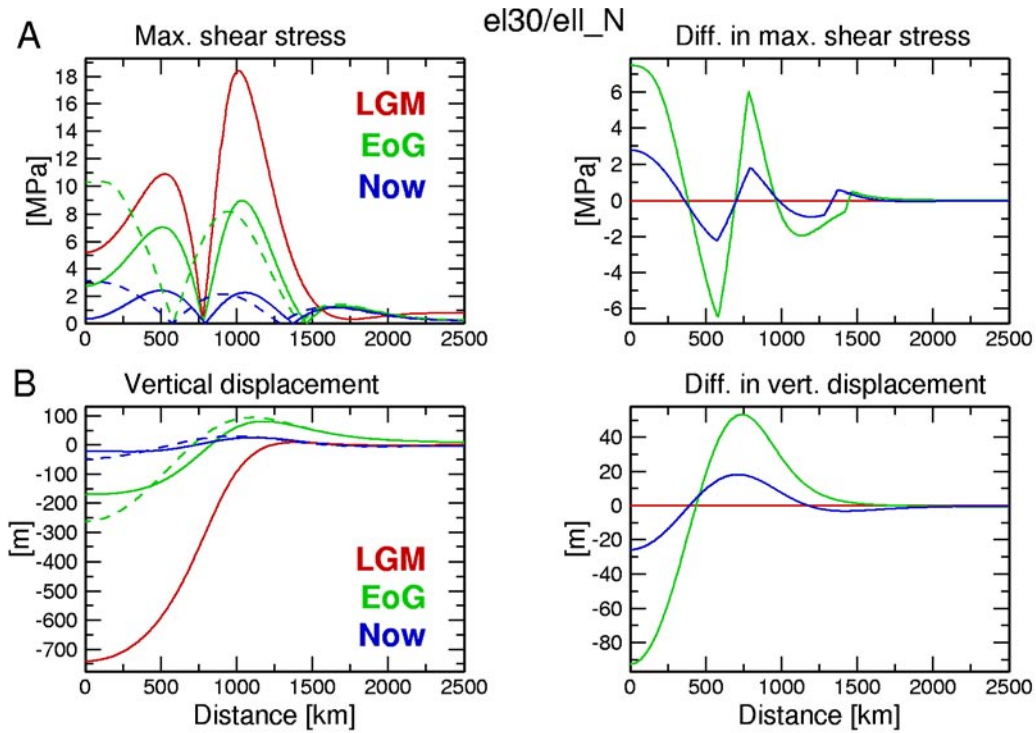
7.2   Non-stationary, elliptic ice model

In order to investigate how the Earth response changes if we model the deglaciation process more realistically than by just letting the height decrease over a constant area, we construct an ice model which decrease both in height and lateral extent during deglaciation. This is an elliptic ice model, which at the start of the glaciation occupies the entire 900 km of lateral extent and grows linearly in height until the LGM. During deglaciation, however, the ice volume (or area) is decreased linearly from its LGM value to zero over 10 kyr in 0.5 kyr intervals. At each 0.5 kyr point, the ratio of maximum height to lateral extent is kept constant and in the 0.5 kyr intervals the pressure amplitude is linearly interpolated. We show in Figure 7-3 the extent of the ice at 10 time intervals between LGM and EoG.

In Figure 7-4 we show the resulting shear stress distributions and vertical displacements at the surface. Since the ice loading is identical for the two ice models there is no difference in the LGM responses. However, at EoG and present time, we see that the retracting ice model produces a very different response than the stationary ice model. The location of maximum shear stress migrates toward the center of the ice and the magnitude is higher than for the reference model. There is significantly more vertical displacement below the center of the (former) ice sheet and the forebulge has also moved toward the center. The non-stationary ice model also leaves more residual rebound at present time. Comparing the shear stress distributions in the entire elastic plate in Figure 7-5 and Figure 2-6, we, again, observe the marked shift of the inner maxima toward the center of the ice at EoG and at present time. The maximum magnitude is higher for the non-stationary ice and the location of the maximum has shifted from the outer maximum to the inner maximum. There is less difference in the stress states, using the non-stationary ice moves the border between thrust and normal faulting further toward the center at EoG and at present.
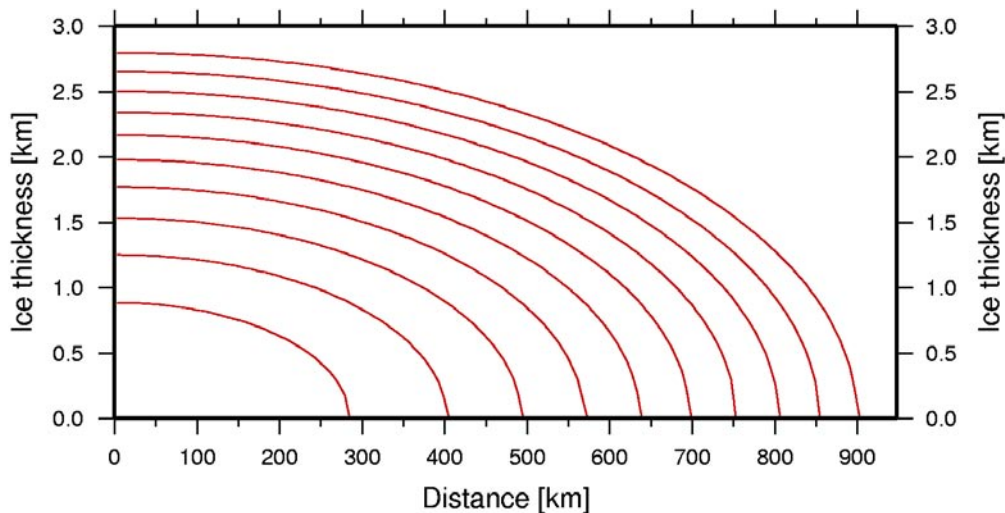
Figure 7-3. *Evolution of the non-stationary, elliptic cross-section ice model. At LGM the ice is identical to that of the reference model ice sheet. Ice cross-sections with 1 kyr intervals are shown in the figure, from the maximum at LGM, 18 kyr BP, to 9 kyr, BP. At 8 kyr the ice has disappeared.*

Figure 7-4. *A) Maximum shear stress and B) vertical displacements for the reference model and the model ell_N with the non-stationary, elliptical ice model. Lines and colours as in Figure 4-1.*
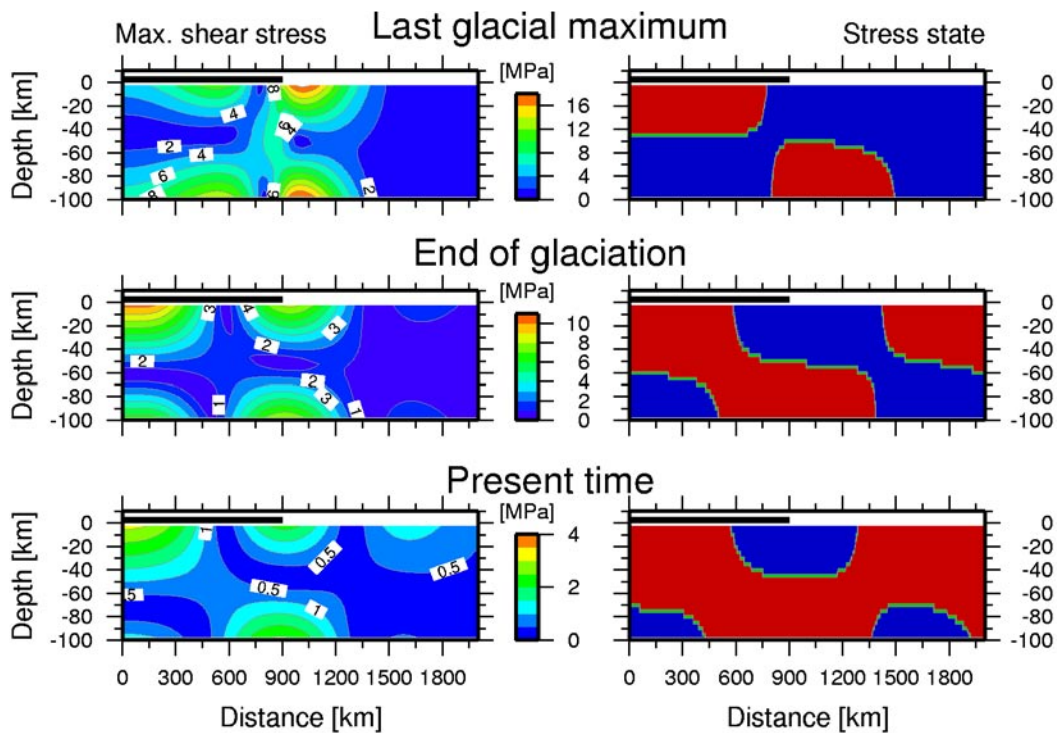
Figure 7-5. *Contour plots of maximum shear stress, left, and state of stress, right, for the model with a non-stationary ice model (Figure 7-3). Stress states are coloured as; extension (blue), strike-slip (green) and thrust (red). Lateral distance from the center of the ice load versus depth. Three different times are shown, LGM at the top, end of glaciation in the middle and present time, bottom. The black bar on top of the plots indicate the extent of the ice at LGM.*

8　Glacial rebound and fault stability

In the preceding sections we have investigated the Earth's response, in terms of stress and displacements, to variations in the earth and ice models. In order to understand how these variations affect the possible reactivation of faults we need a fault stability criterion, and we will concentrate on the criterion most widely used in Earth Science applications, the Mohr-Coulomb criterion. This section will briefly describe the Mohr-Coulomb criterion and two variations in its application to endglacial faulting. Fault stability will be then be investigated for three different variations of earth and ice models and the importance of initial stress and pore pressure will be discussed. The section closes with a brief discussion on the inclusion of Mohr-Coulomb plasticity as a material property in the models.

8.1　Mohr-Coulomb frictional failure theory

The Mohr-Coulomb (or Coulomb or Coulomb-Navier) criterion relates the maximum shear stress, τ, and the normal stress, σ_n, on a fault plane in a brittle material through the coefficient of friction, μ, and the cohesion S_0:

$$\tau = \mu(\sigma_n - P_f) + S_0 \tag{7}$$

where P_f is the pore fluid pressure. The Coulomb criterion is an empirical relationship which only involves the maximum and minimum principal stresses and, thus, disregards any influence of the intermediate principal stress on the initiation of faulting. When considering pre-existing faults at depth in the crust, the cohesion term is insignificant and usually ignored. For a fault whose normal is at an angle θ to the maximum principal stress, S_1, the shear and normal stresses on the fault is given by:

$$\tau = \frac{S_1 - S_3}{2} \sin(2\theta) \tag{8}$$

and

$$\sigma_n = \frac{S_1 + S_3}{2} + \frac{S_1 - S_3}{2} \cos(2\theta) \tag{9}$$

where S_3 is the minimum principal stress. The coefficient of friction can be written as $\mu = \tan(\varphi)$, where φ is the angle of friction. If the plane has the orientation $\theta = \varphi/2 + \pi/4$, it will be the first plane on the Mohr-circle to reach the failure envelope and is, consequently, referred to as optimally oriented. Combining Equations 7–9 gives:

$$\frac{S_1 - P_f}{S_3 - P_f} = \left(\sqrt{\mu^2 + 1} + \mu\right)^2 \tag{10}$$

/Jaeger and Cook, 1979/. This equation is convenient for predicting the differential stress necessary to cause fault instability at depth.

Relationships between the shear and normal stress on a fault, fault orientation and the principal stresses are straightforwardly illustrated by a Mohr diagram, see Figure 8-1, where stresses are denoted σ but we will use S below. We can clearly see how the semi-circle defined by the maximum and minimum principal stresses approach the failure envelope as differential stress, $S_1 - S_3$, is increased and how the circle recedes from failure as the mean stress, $S_1 + S_3$, is increased. Pore fluid pressure reduces the mean stress, which in the Mohr diagram moves the circle to the left and, thus, again approach failure. In the Mohr diagram we have also illustrated the two fault stability measures used in this study. The fault stability margin, FSM, /Quinlan, 1984; Johnston, 1987/ is the distance in Mohr-space from a fault's position on the Mohr-circle to failure, orthogonal to the failure envelope, see Figure 8-1:

$$FSM = \beta \left[\mu(S_1 + S_3 - 2 P_f) + 2\, \tau_0 \right] - \frac{1}{2}(S_1 - S_3) \tag{11}$$

where $\beta = \sin(\mathrm{atan}(\mu))/2\mu$. The instability measure, used e.g. by /Lund and Slunga, 1999/, is similar but simply the vertical distance to the failure envelope from a fault's position on the circle, see Figure 8-1:

$$Instab = \tau - \mu(\sigma_n - P_f) - S_0 \tag{12}$$

We note that the FSM is calculated for an optimally oriented fault whereas the Instab measure is applicable to any fault. We also see that for a fault to become unstable, the FSM path requires a decrease in fault normal stress as well as an increase in shear stress, which is achieved if the differential principal stress increases while the mean stress is constant. The Instab path, on the other hand, only considers an increase in fault shear stress for a given fault normal stress, i.e an increase in differential principal stress accompanied by a suitable increase in mean stress.

In a series of papers /e.g. Wu and Hasegawa, 1996a,b; Wu, 1997; Wu and Johnston, 2000/, Wu has analyzed the influence of rebound stresses on fault stability using the FSM measure. Noting the uncertainty in the values for μ, S_0, P_f, and the crustal deviatoric stress, Wu settled on using a differential measure of the FSM. The dFSM is the difference between the FSM at two different points in time, usually involving two different stress fields. Defined as

$$dFSM(t) = FSM(t) - FSM(t_0) \rightarrow$$
$$\frac{1}{2}\left[\left[S_1(t_0) - S_3(t_0) \right] - \left[S_1(t) - S_3(t) \right] \right] + \mu\beta \left[\left[S_1(t) + S_3(t) \right] - \left[S_1(t_0) + S_3(t_0) \right] \right] \tag{13}$$

dFSM is positive if faults are more stable at time t than at the reference time t_0, and negative if fault failure is promoted. We note that for a time invariant μ, dFSM is independent of pore pressure, cohesion and the weight of the overburden if these quantities are also time invariant. We also note that since FSM applies to optimally oriented faults, we are not comparing the same faults at time t and time t_0 but rather the generic stability of faults. There is, however, a problem associated with dFSM when assessing the stability of faults. Due to it's nature as a differential measure, dFSM will correctly predict the increased/decreased stability of faults as the stress field evolves. It will not, however, indicate whether or not the faults are close to failure. For such an assessment an absolute measure of fault stability have to be utilized.

Below we will investigate how fault stability is affected by rebound stresses using both the dFSM and Instab measures. This will enable us to compare the merits of the two approaches and how they best add to our understanding of endglacial faulting.
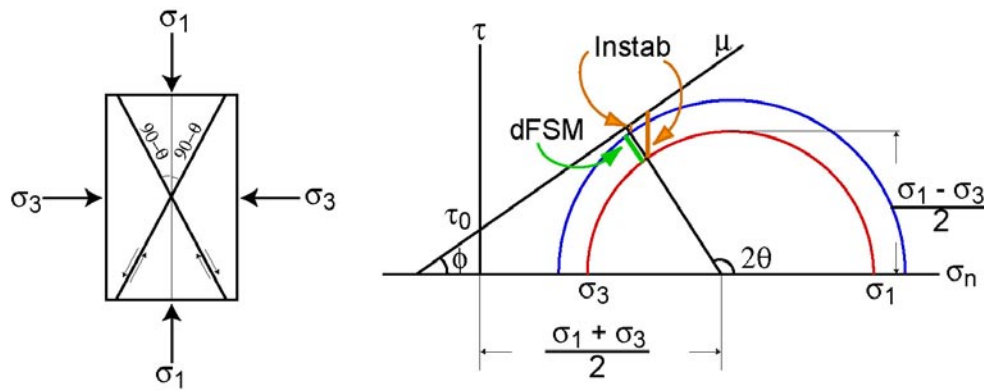
Figure 8-1. *Left: Angular relationship between failure planes and principal stresses. Right: Mohr circles for two different states of stress, red and blue. The Instability measure is indicated by the two orange lines, dFSM by the green line.*

8.1.1 Pore pressure

In the model results presented above we have not incorporated effects of fluids. We know that the lithosphere to a large extent is saturated by fluids and that the pore pressure that these fluids exert reduce normal stresses in the Earth. Since it is these reduced, or effective, stresses that act to cause fault failure, as we saw in Eqns 7 and 10, inclusion of pore pressure in the modelling of endglacial faulting is crucial. In order to include pore pressure in our modelling in a "correct" manner we have to use a finite element formulation that allows pore fluid movement. This is straightforwardly done in our modelling software Abaqus, as it is equipped with the proper type of elements. It is, however, difficult to find simple models of GIA with pore fluids that we can validate our model against. We will use the Decovalex projects /e.g. Wallroth et al. 2002/ results, which incorporated pore fluids in glacial rebound models but only use elastic media. GIA with pore fluids in viscoelastic media are more elusive. We have, therefore, so far not included pore pressure on the element level in the modelling. This is, however, an important and necessary development of the model since it will allow us not only to reduce the differential stress necessary to cause fault instability but also to incorporate dynamic pore fluid effects as the ice evolves.

From a stress point of view, a simple way to include a static pore fluid pressure is by reducing the density of the rock, thereby accounting for the decrease in normal stress caused by the fluids. Assuming hydrostatic conditions in the elastic part of our reference model would decrease the density from 3,380 kg/m³ to 2,380 kg/m³. Unfortunately, this is not possible from the GIA modelling viewpoint. We saw in section 4.3 how the shear stress of the reference model was affected by a decrease in elastic plate density from 3,380 to 2,730 kg/m³. The buoyancy mode of the isostatic adjustment process is sensitive to density variations like these and a lowering of the model density is, thus, not a viable way to achieve pore pressure effects.

Another possibility to include pore pressure effects is to assume that they are insignificant to the rebound stress modelling, an assumption which may be incorrect if dynamic effects are incorporated, and only include them as static effects on fault stability in the postprocessing stage. We have chosen this method in the section on deviatoric initial stresses below, where a deviatoric stress state is calculated assuming a certain pore pressure. This deviatoric stress is added to the result of the rebound stress modelling and the sum of the stresses then assessed from a faulting perspective, again including a static pore pressure as dFSM and Instab is calculated. Noting that the elastic part of the model, where the deviatoric stress is applied, lacks any plastic behaviour to relax stresses, this approach to pore fluid pressure inclusion is valid for this particular model.

47

8.1.2 Initial state of stress

It is well known from e.g. earthquake focal mechanisms, borehole measurements and geology that the ambient state of stress in the lithosphere is not simply equal to the weight of the overburden /e.g. Zoback, 1992/. There is, in most areas, a significant deviatoric component added to the isotropic overburden stress. In addition, there is three independent lines of evidence indicating that the state of stress in intraplate continental upper crust is in frictional failure equilibrium: (1) seismicity induced by fluid injection or reservoir impoundment; (2) seismicity induced by other earthquakes and; (3) in situ stress measurements in deep boreholes /see e.g. Zoback and Townend, 2001, for references/. Measured stresses are frequently found to be approximately equal to those predicted by Coulomb frictional failure theory /e.g. review in Townend and Zoback, 2000/, using laboratory derived coefficients of friction of 0.6–1.0 /Byerlee, 1978/.

The above mentioned circumstances indicate that a careful inclusion of the initial state of stress is very important if we are to properly assess fault stability in the varying stress field created by the GIA processes. Below we will show how the fault stability measures are affected by the initial stress, using zero, isotropic and deviatoric initial stresses.

8.2 Glacial rebound and faulting

In this section we will show some examples of how the stresses induced by glacial rebound affect the stability of faults, using the Instab and dFSM measures discussed above. We will consider three different models: our reference model with a 100 km thick elastic plate, the model lay2 of section 4.5, which differs from the reference model by having a 50 km thick elastic plate, and the reference earth model with the non-stationary ice of section 7. In the discussion below these models will be referred to as model m1, m2 and m3 respectively. The models will be investigated using three different initial stress states: first with no initial stress in order to understand how the rebound stresses are reflected by our fault stability measures; then an isotropic initial stress and finally a deviatoric initial state of stress with the upper crust in frictional equilibrium on optimally oriented faults, with a coefficient of friction of 0.6. We recall that the ice has a lateral extent of 900 km and exerts a maximum pressure of 25 MPa below the centre, decreasing elliptically toward the ice margin. LGM is at 18 kyr BP and the ice disappeared at 8 kyr BP in models m1 and m2, and gradually decreased from 18 to 8 kyr BP in model m3. Stresses and fault stability are displayed for 2.5 km depth at four different locations in the plots below: 500, 750, 900 and 1,050 km from the ice center. We see from e.g. Figure 2-6 that these locations correspond to the inner maxima in shear stress, the shear stress minimum, the edge of the ice and the outer shear stress maximum, respectively. We also note, from the ice history in Figure 7-3, that the non-stationary ice of model m3 disappears from the 750 km point between 15–14 kyr and from the 500 km point between 11 and 10 kyr. We have chosen to show the maximum horizontal, SH, and vertical, Sv, stresses below. It should be noted that although these correspond to the directions of the maximum, S1, and minimum, S3, principal stresses in most of the model, there is a region, central in the plate below the ice margin, where there are significant shear stresses. Also, the directions of S1 and S3 are interchanged as we move along the model, cf. Figure 2-6, implying that SH is sometimes equal to S1 and sometimes to S3. Finally, we point out that the models, as used in this section, do not contain plasticity in the elastic plate, i.e. the models will not deform plastically in response to stresses above the fault stability threshold and these stresses will, consequently not be relaxed by the model. In section 8.3 below we will briefly consider plasticity.

8.2.1   Stress free initial state

We start by studying only the incremental stresses from the rebound process and their influence on our faulting measures. In Figure 8-2 we show the maximum horizontal and vertical stress for the three models and four locations. As expected, the horizontal stress in models m1 and m3 are identical up to LGM due to the identical earth and ice models thus far, and all three models have, almost, identical vertical stresses until LGM. Only at the ice margin does the thin plate model m2 have slightly higher vertical stress than m1 and m3. We see, again, that the glaciation produce high horizontal incremental stresses, at 500 km for models m1 and m3 the ratio of horizontal to vertical stress is approximately two, the difference being approximately 20 MPa. As discussed in section 4.5 and Figure 4-10, we note again that model m2 has its maximum and minimum shear stress areas offset toward the ice edge. Figure 8-2 clearly show how the horizontal stress vary from compressive under the ice to tensional in the forebulge region, and that the magnitude of the maximum tensional SH is approximately half of the maximum compressional SH. We also see the large impact the non-stationary ice model has on the stress evolution, specially under the ice. As discussed in section 7, the receding ice amplifies stress under the central areas of the ice and then decrease stress magnitudes faster than the stationary ice as the ice margin passes. Finally, as noted earlier, all models show residual stress today.

Turning now to the Instability and dFSM measures in Figure 8-3, we recall from the definitions that positive Instability implies fault reactivation whereas negative is more stable faults. dFSM, on the other hand, promotes stability with positive values and promotes faulting with negative values. /Wu, 1996a/ points out that for the dFSM measure to be of interest, the optimally oriented faults must be considered as critically stressed at the onset of glaciation. This assumption is not compatible with the assumption of zero initial stress, obviously, but it is nevertheless useful for the presentation of the rebound stresses.

We see how, during the glaciation phase, stability is promoted by the dFSM measure under the ice sheet but that outside the ice faulting is strongly promoted. The Instability measure similarly shows that there is no faulting under the ice but that outside the ice sheet faulting should be abundant. These observations are consistent with those of /Johnston, 1989/, who demonstrated that, for an elastic model, the presence of a large ice sheet tends to suppress seismic activity. As deglaciation starts, we see that under the ice sheet the stability measures both indicate that faults become increasingly less stable. When the mean stress, i.e. the average of the principal stress magnitudes, becomes small enough compared to the differential stress, the faults become unstable. We see that this generally happens before deglaciation is complete. We also note that the maximum measures of instability are generally reached as the ice disappears. Faults in our reference model m1 are predicted to become unstable at approximately 13 kyr BP at 500 km, and at 9 kyr BP at 750 km. The non-stationary ice of model m3 significantly increases the magnitude of Instability or dFSM, and at the same time decreases the time from LGM to the onset of fault instability, this is especially noticeable at 750 km. Comparing Figure 8-2B and Figure 8-3B, we note that the large increase in Instability/decrease in dFSM occurs as the ice of model m3 recedes from 750 km and the state of stress changes from reverse faulting to normal faulting. It should be noted that as the stress state changes, the orientation of the optimally oriented faults change as they follow S1. In the case above we go from studying faults dipping 30 degrees to faults dipping 60 degrees. After the completion of deglaciation, viscoelastic relaxation causes both stability measures to tend slowly toward zero. Outside the ice sheet both measures indicate that the model continues to be unstable during the entire deglaciation process. This is due to the tensional horizontal stress not being matched by any increase in the vertical stress, i.e. the differential stress increase much more than the mean stress.
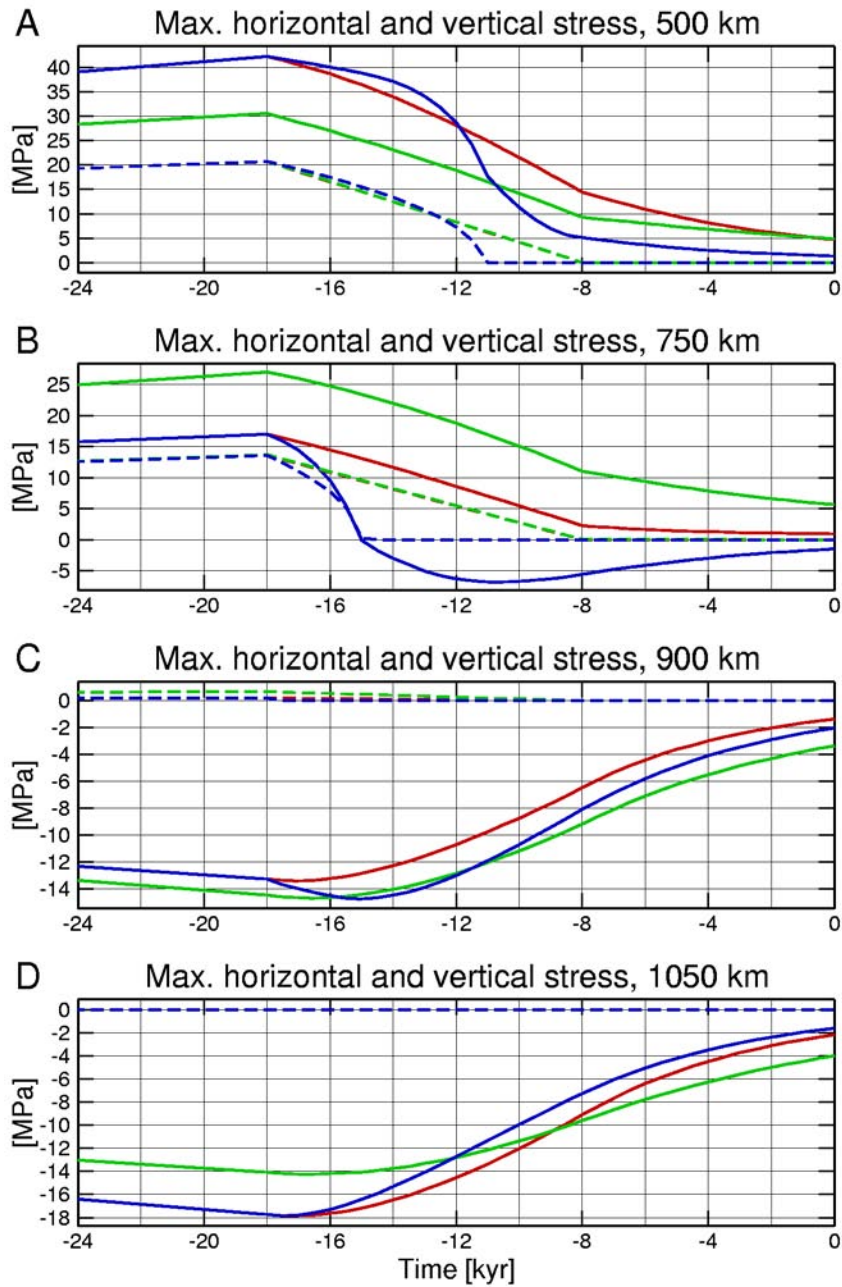
Figure 8-2. *Horizontal, solid lines, and vertical, dashed lines, stresses at 2.5 km depth versus time in kyr BP. The stresses are incremental rebound stresses only. Model m1 in red, model m2 in green, model m3 in blue. Stresses investigated at A) 500 km, B) 750 km, C) 900 km and D) 1,050 km from the center of the ice load.*
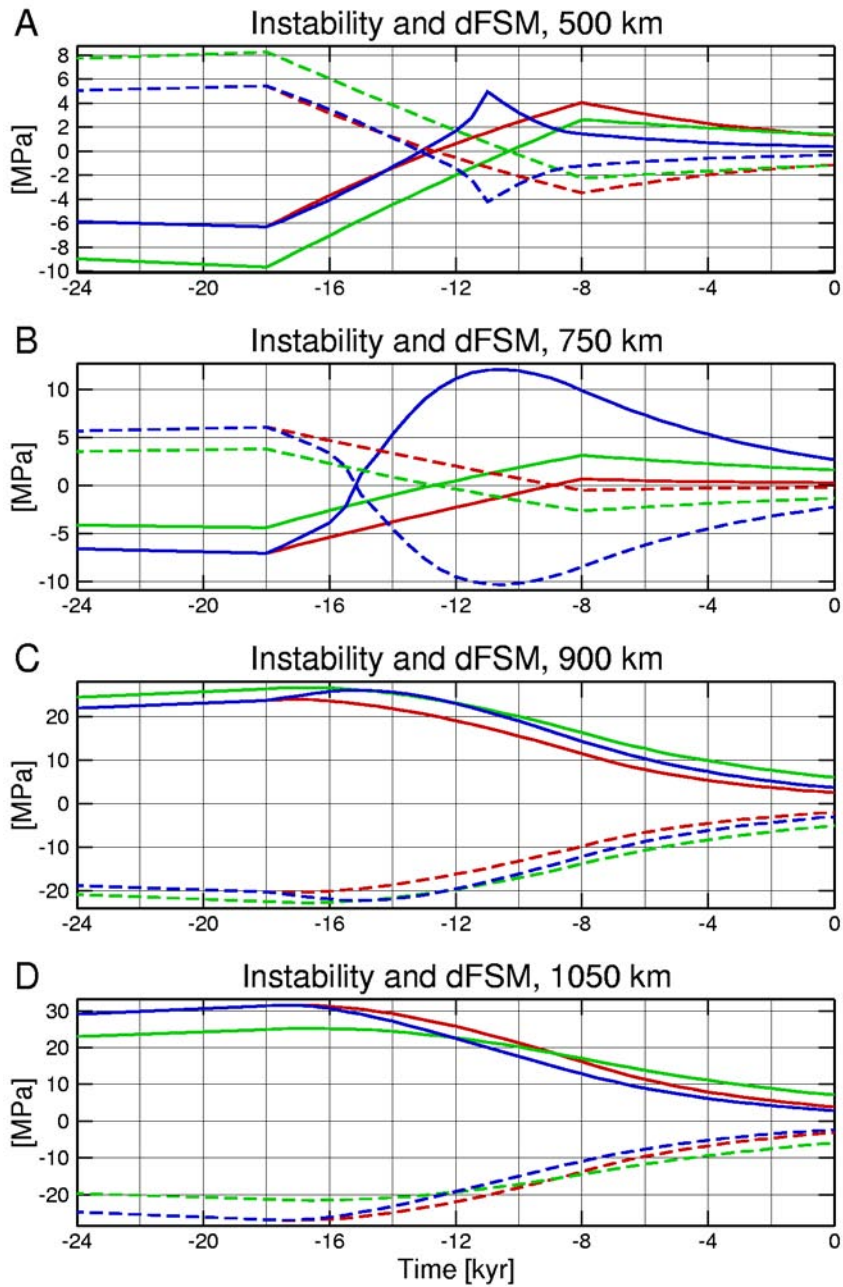
Figure 8-3. *Instability, solid lines, and dFSM, dashed lines, at 2.5 km depth versus time in kyr BP. Model m1: red, m2: green, m3: blue. Distances as in Figure 8-2.*

In Figure 8-4 we have plotted Instability and dFSM for the entire first 2,000 km of the model versus time. The depth of evaluation is again 2.5 km for model m1 and m3, but 1.25 km for model m2. These depths correspond to the center of the first row of finite elements. We now observe more clearly the patterns outlined above, i.e. how the ice sheet promotes stability under the ice but instability outside, specially in the forebulge region. We also see how a thinner elastic plate produces a more localized region of fault instability outside the ice sheet, and that the non-stationary ice decreases the time to instability below the outer regions of the (former) ice sheet and increases the magnitude of the fault stability measure. We note that these models show fault instability at all times outside the ice edge.

We conclude this section by again stressing that the above discussion only pertains to the rebound stresses. The inclusion of overburden and crustal scale deviatoric stresses will significantly change some of the conclusions of this section.
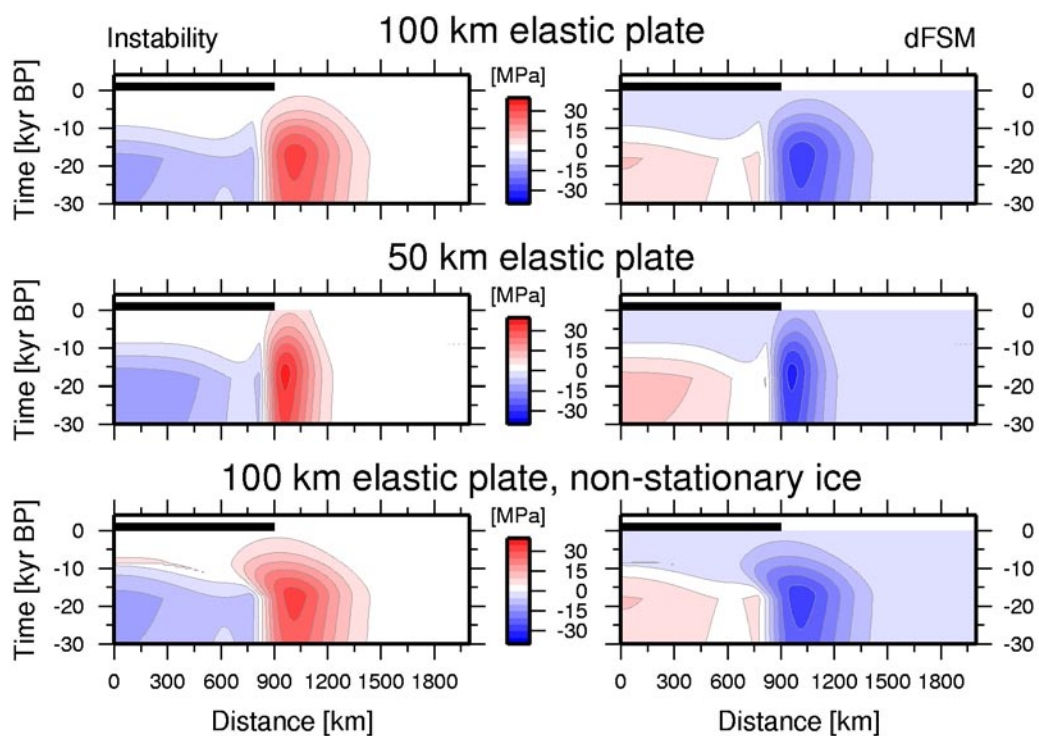
Figure 8-4. *Contour plots of Instability and dFSM for models m1, top, m2, middle, and m3, bottom, at depth 2.5 km for m1 and m2 and 1.25 km for m3. Note that the zero contour is between white and blue. Models only include rebound stresses. Distance from the center of the ice load versus time, in kyr BP. The black bar on top of the plots indicate the extent of the ice at LGM.*
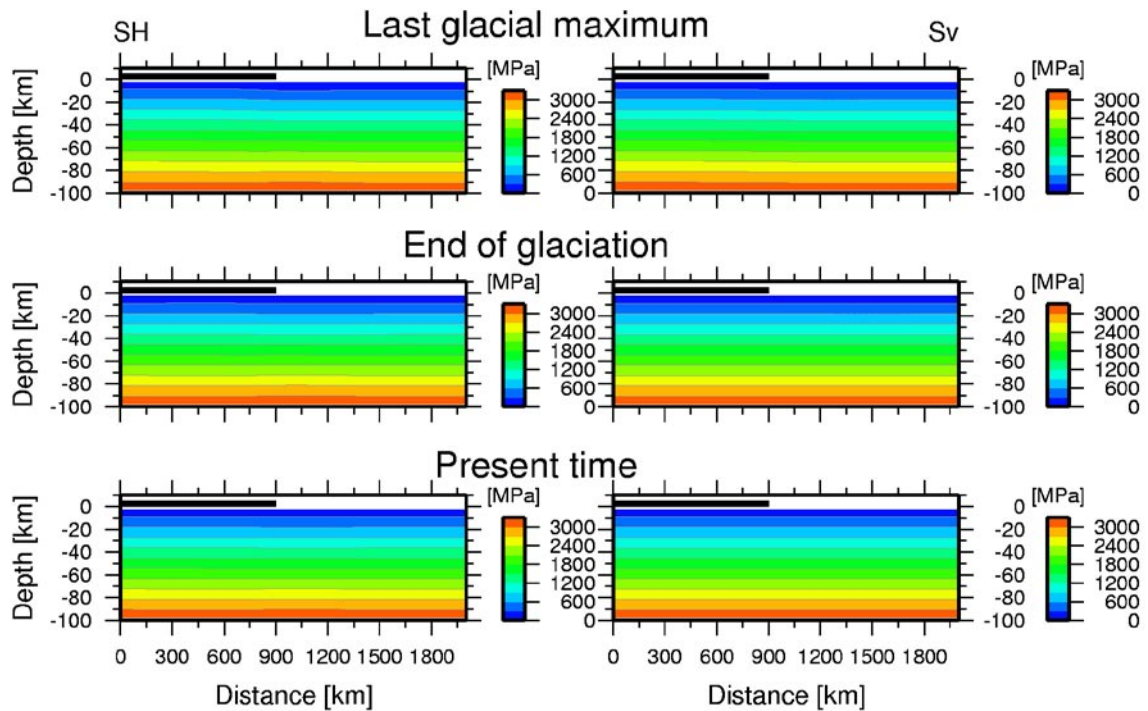
Figure 8-5. *Contour plots of the maximum horizontal, left, and vertical, right, stresses for model m1 including the weight of the overburden. Time slices at LGM, EoG and present. Distance from the center of the ice load versus depth.*

## 8.2.2 Isotropic initial stress: the weight of the overburden

In this section we will make our study of the effect of the rebound stresses on fault stability slightly more realistic by including the isotropic weight of the overburden in the models. Using our model's density of 3,380 kg/m^3, the mean stress in the model increases by 33 MPa/km. It is instructive to compare this gradient to the maximum horizontal stress produced by the glaciation, approximately 45 MPa at 2.5 km depth. We see that already at 2.5 km depth, the glacially induced horizontal stress is only 50% of the overburden stress and as we proceed deeper into the model the rebound stresses will become relatively insignificant. In Figure 8-5 we show the maximum horizontal and the vertical stresses for the model m1 including the weight of the overburden. We see that differential stresses are virtually undetectable at these scales.

Figure 8-6 shows the horizontal and vertical stresses at the four locations discussed above, and we see that the curves are identical to those in Figure 8-2, except for the added 83 MPa of overburden stress.

Turning to Figure 8-7, we encounter the above mentioned problem of dFSM as a differential measure. The dFSM measures in Figure 8-7 are identical to those of Figure 8-3, indicating that exactly the same tendencies for fault stability/instability apply when the overburden is included in the models. The Instability measure, however, shows that although there are variations in the tendency toward increased or decreased stability, the verburden effectively prohibits all fault instability everywhere in the model by a massive increase of the normal stress. Inserting numbers in Eq 12, we note that the Instability measure in the initial, isotropic, state has a value of Ins = 0 − μ(S1 + S3)/2 = –49.7 MPa, which is what the Instability measure tends toward during the viscoelastic relaxation.

In order to show the effect of the overburden even more explicitly, we include a Mohr circle diagram of the state of stress at the 500 km location at 11 kyr BP, see Figure 8-8. We see that the Mohr circles (the differential stresses) are tiny and very far away from the failure envelope, although the dFSM measure shows that models m1 and m3 are now promoting fault failure.

These examples show that careful interpretation of the dFSM measure is necessary when discussing fault stability, and also that careful language consideration needs to be taken not to confuse "promoting fault instability" with "fault instability".
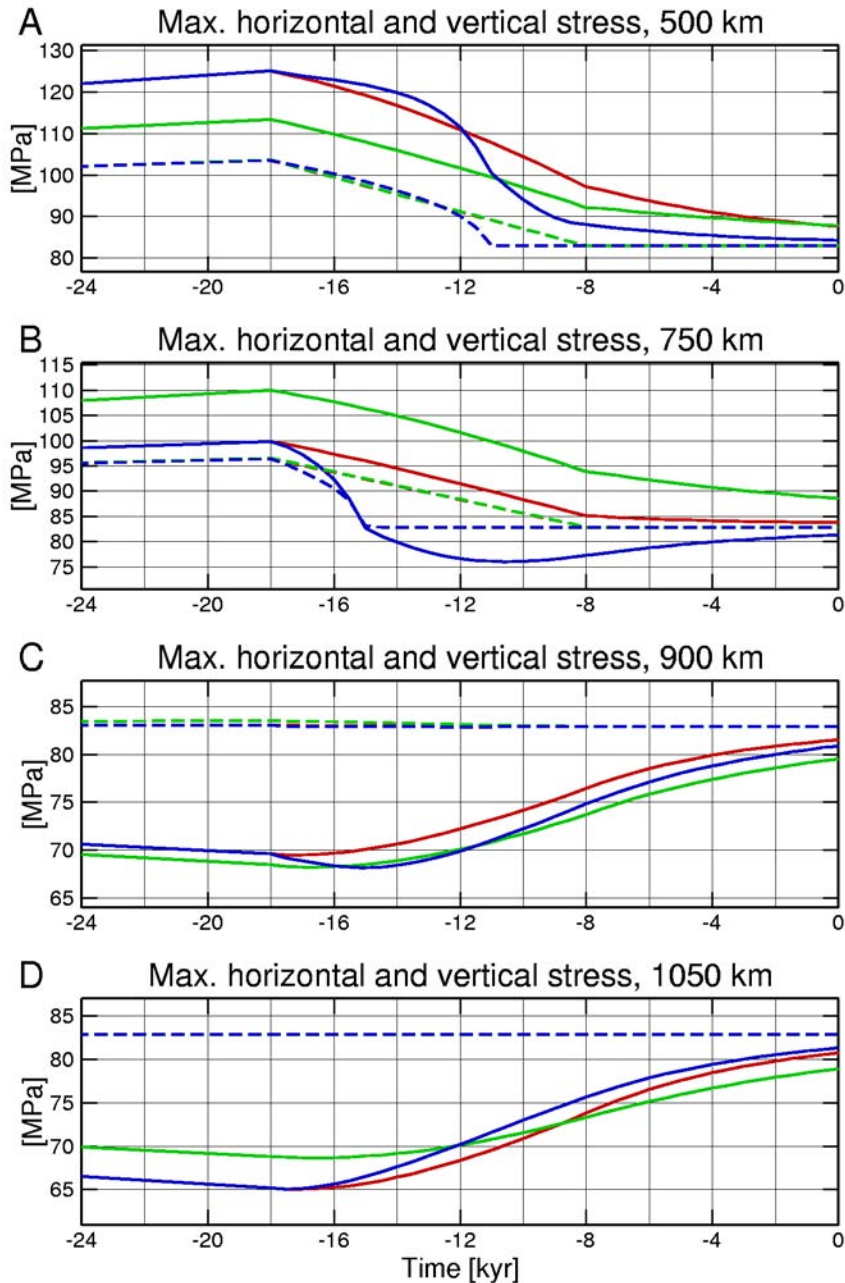
Figure 8-6. *Horizontal, solid lines, and vertical, dashed lines, stresses at 2.5 km depth versus time in kyr BP. The stresses are incremental rebound stresses with the weight of the overburden added. Model m1: red, m2: green, m3: blue. Distances as in Figure 8-2.*
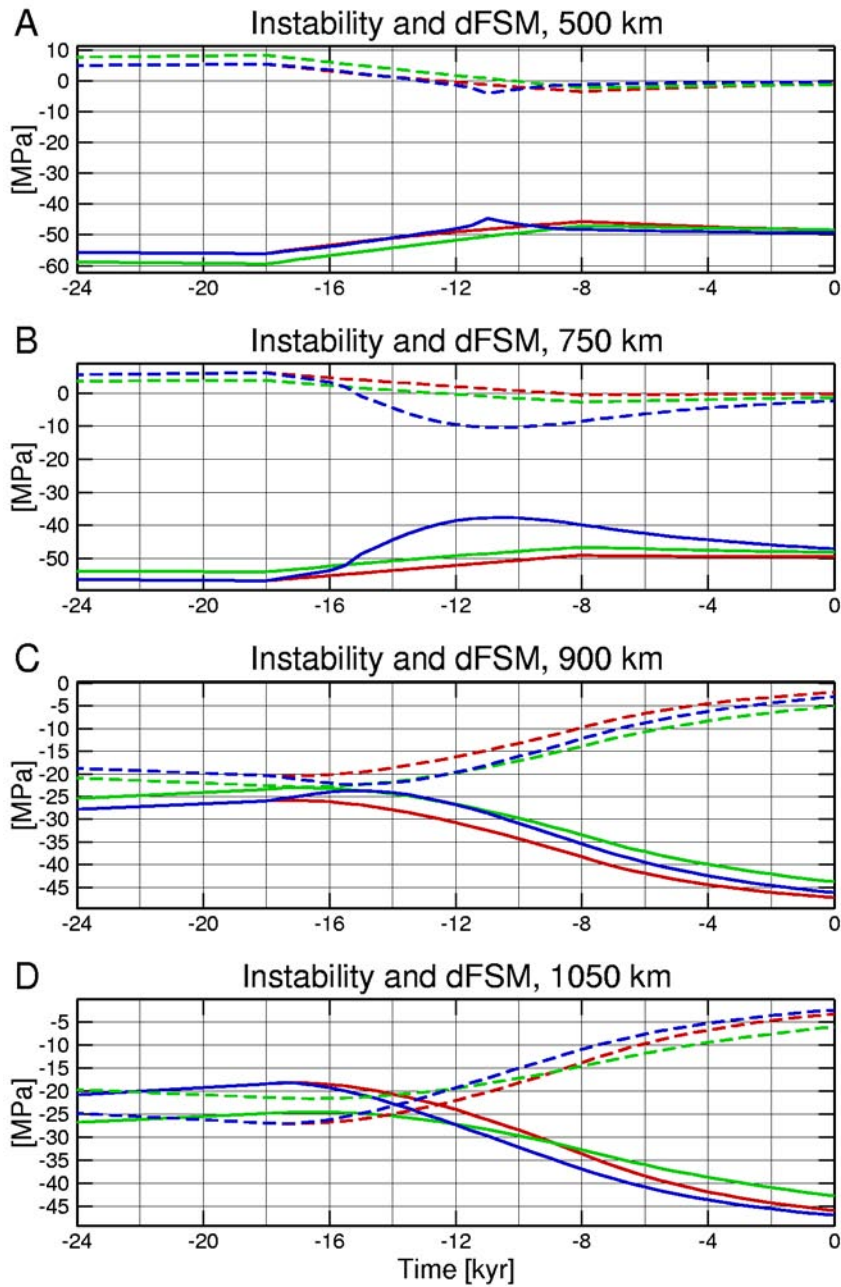
Figure 8-7. *Instability, solid lines, and dFSM, dashed lines, at 2.5 km depth versus time in kyr BP. Models include the weight of the overburden. m1: red, m2: green, m3: blue. Distances as in Figure 8-2.*
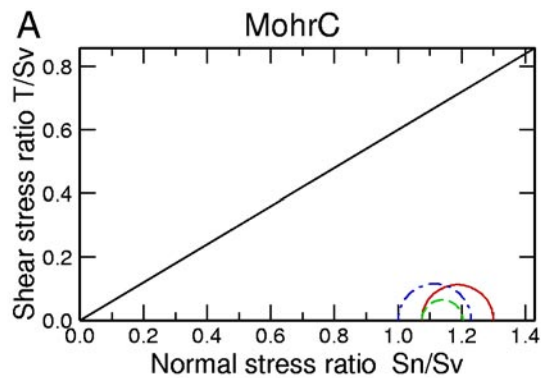
Figure 8-8. *Mohr diagram with the maximum and minimum principal stresses, scaled by the vertical stress, at 500 km from the load center and 11 kyr BP. Model m1: red, m2: green, m3:blue. Rebound stress plus overburden weight. Coefficient of friction is 0.6.*

8.2.3 Deviatoric initial stress: the critically stressed crust

In order to model a more realistic initial stress field we add a deviatoric stress tensor to the weight of the overburden. As discussed above, we have not been able to include pore pressure in the modelling proper. However, since our models do not include plasticity in the elastic plate at this stage, the entire deviatoric stress study can be undertaken as a postprocessing operation on the modelled rebound stresses, and we can then "artificially" consider a non-zero pore pressure. In this study pore pressure is taken into account both when constructing the deviatoric stress field and in the evaluation of the fault stability measures. Using a static pore pressure of 40% of the vertical stress (slightly above hydrostatic) and a coefficient of friction of 0.6, we construct a reverse faulting deviatoric stress field, using Eq 10, in frictional failure equilibrium on optimally oriented faults. Following /Zoback and Townend, 2001/ we limit the strength of the plate to approximately the value inferred for the cumulative strength of the lithosphere, 1–4 10^12 N/m /Forsyth and Uyeda, 1975; Bott and Kusznir, 1984; Kusznir, 1991/. Applied to our discontinuous models this implies that the deviatoric stress field is confined to the upper 15 km of the elastic plate. Below 15 km the initial stress field is isotropic (we note that our Maxwell viscoelastic half-space cannot be initialized to a deviatoric stress since it does not have any long term strength).

In Figure 8-9 we plot the horizontal and vertical stresses at 2.5 km depth and we see that the horizontal stresses are now a factor of approximately two higher than the vertical stress. Before considering the entire time variations of the Instability and dFSM measures we, again, view the Mohr diagram at 500 km, 2.5 km depth and 11 kyr BP, see Figure 8-10. We now see that the initial states of critically stressed, optimally oriented faults, have evolved during glaciation and partial deglaciation into stress states where optimally oriented faults in models m1 and m3 would fail.
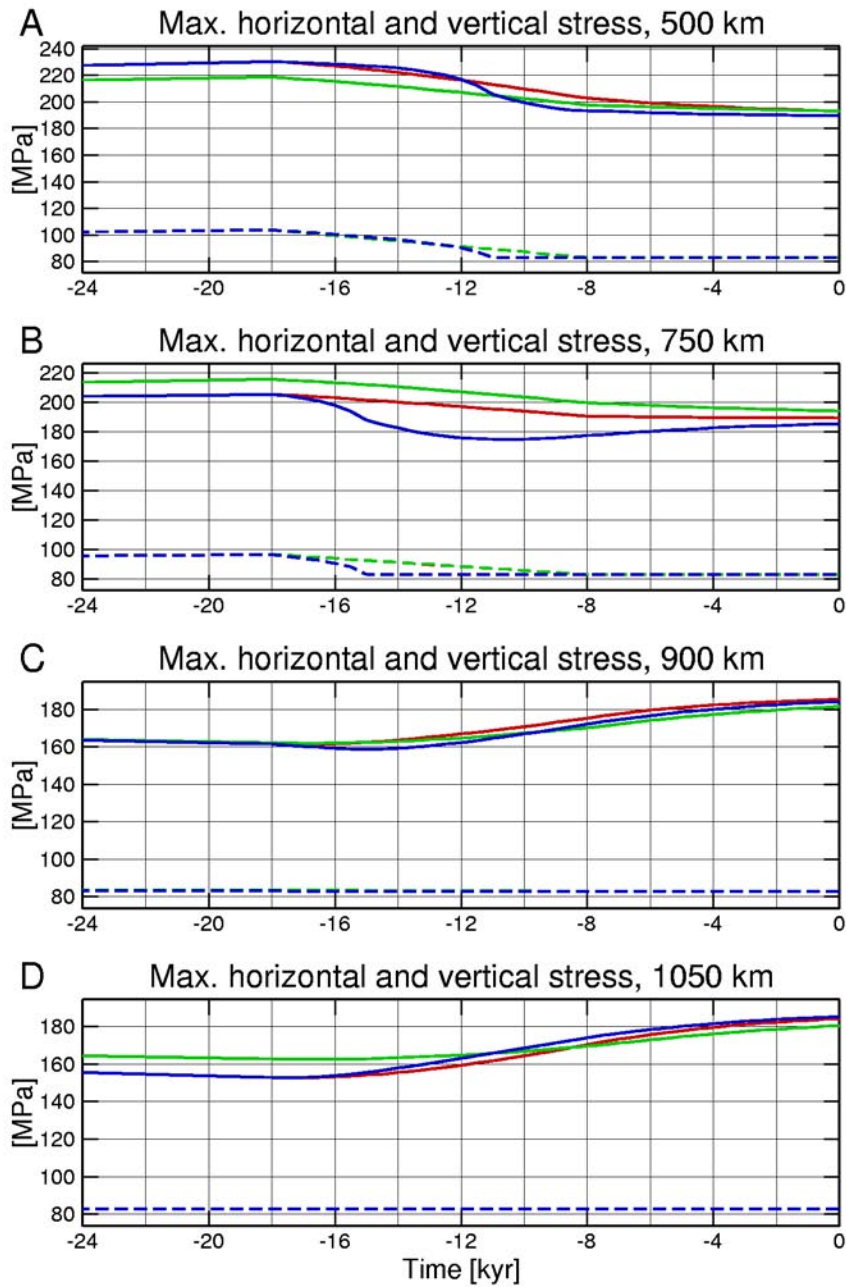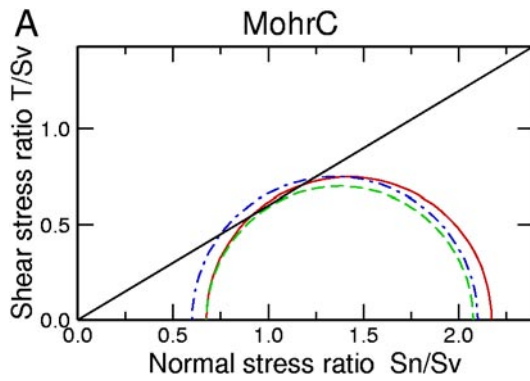
Figure 8-9. *Horizontal, solid lines, and vertical, dashed lines, stresses at 2.5 km depth versus time in kyr BP. The stresses are incremental rebound stresses with the weight of the overburden and a deviatoric component added. Model m1: red, m2: green, m3: blue. Distances as in Figure 8-2.*

Figure 8-10. *Mohr diagram with the maximum and minum principal stresses, scaled by the vertical stress, at 500 km from the load center and 11 kyr BP. Model m1: red, m2: green, m3:blue. Rebound stress plus overburden weight and a deviatoric component. Coefficient of friction is 0.6.*

Turning to the full time series in Figure 8-11, we note some interesting changes in the stability measures. Comparing Figure 8-11A with its equivalent without initial stress in Figure 8-3A, we note that not only are the dFSM identical, also the Instability measures are equal. We might have expected that the shape of the curves would be identical, as in the case of the isotropic initial stress in Figure 8-7, but not the numbers themselves. This equivalence, however, stems from the fact that although they derive from very different stresses, both examples refer back to a state of Instability equal zero. In Figure 8-3A, because when there are no rebound stresses, all stresses are zero and, thus, Instability is zero, and in Figure 8-11A because we constructed the initial state to be in failure equilibrium, e.g. Instability equals zero. Compare this to the isotropic state above, where initial Instability equals –49.7 MPa. The second effect responsible for the similarity of the figures is the stress state. Both figures are derived from consistently reverse faulting environments. Figure 8-11B and Figure 8-3B shows the effect of stress state reversals. We noted above that the rebound stresses of model m3 change from reverse to normal faulting at 15 kyr BP, at 750 km. With the reverse faulting initial state of this section, however, the small change in the rebound stresses cannot affect the stress state and we see in Figure 8-11B that instead of promoting fault failure, the stability measures turn back toward increased stability before viscoelastic relaxation slowly brings the stresses back toward the initial state. The largest difference between the two different initial states is, however, found for the two locations at and beyond the ice margin. The instability predicted by the zero initial stress models have changed into complete stability during both glaciation and deglaciation. This is due to the tensional horizontal stress produced by the rebound, which acts to decrease the compressive differential stress of the initial state and thus stabilizes the model.
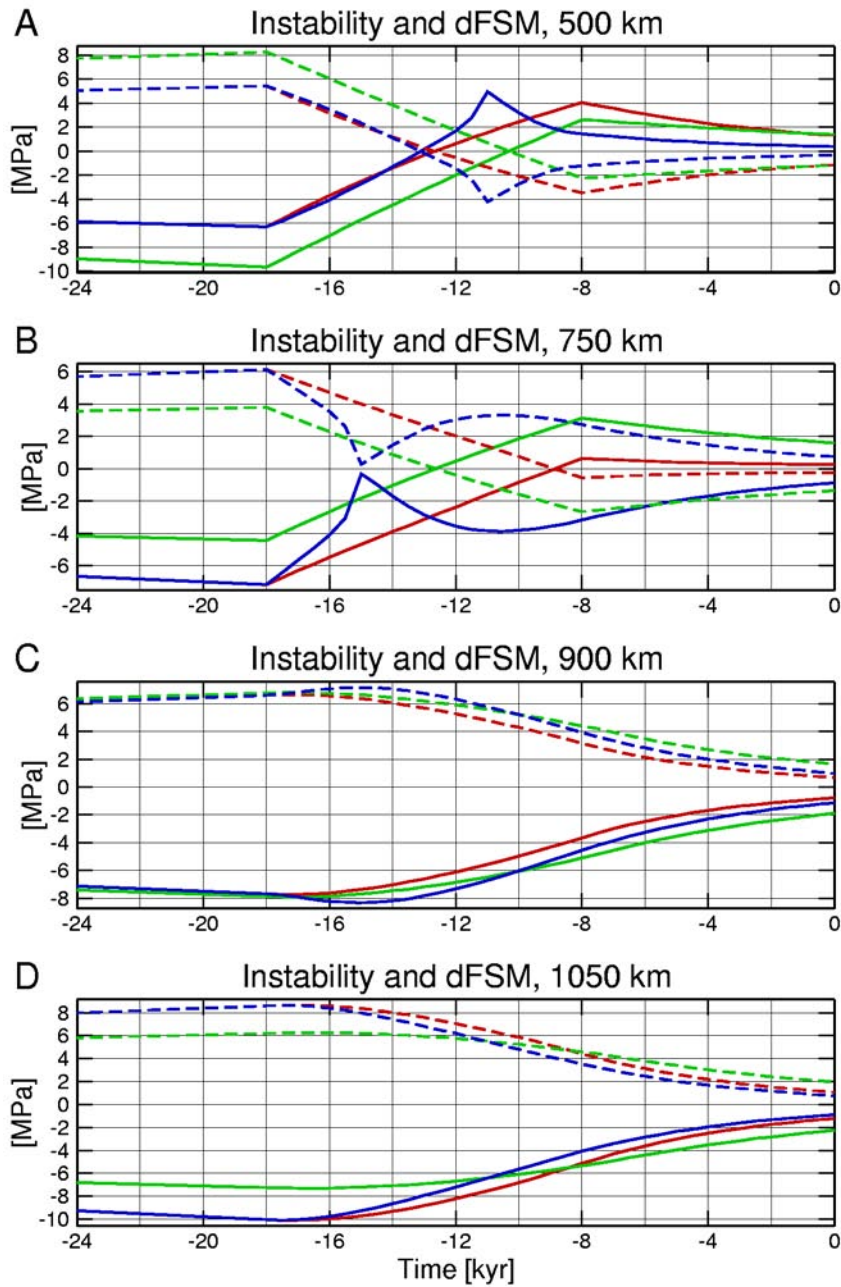
Figure 8-11. *Instability, solid lines, and dFSM, dashed lines, at 2.5 km depth versus time in kyr BP. Models include the weight of the overburden and a deviatoric component. m1: red, m2: green, m3: blue. Distances as in Figure 8-2.*

In Figure 8-12 we, again, show a plot of the stability measures along the entire top of the model at different times. As observed above, we see that in comparison to Figure 8-4 we now have a large region beyond the ice margin that has become stabilized by the initial field during almost the entire glaciation/deglaciation period. Only at times after the final deglaciation is there a region beyond the forebulge which shows increased tendency toward fault failure. The three models show slightly different space-time regions of maximum instability, with the stationary ice models having a region closer to the ice edge than the non-stationary ice model, which shows a motion of the location of maximum instability toward the ice center as time progresses.

An interesting result of the deviatoric, frictional failure equilibrium, initial state example is that it shows that there is complete equivalence between the Instability and dFSM measures of fault stability in this case. Obviously, this can be inferred already from the definitions above, but the current example illustrates it nicely. The example also emphasizes, again, that the initial stress state is very important when assessing the stability of faults.
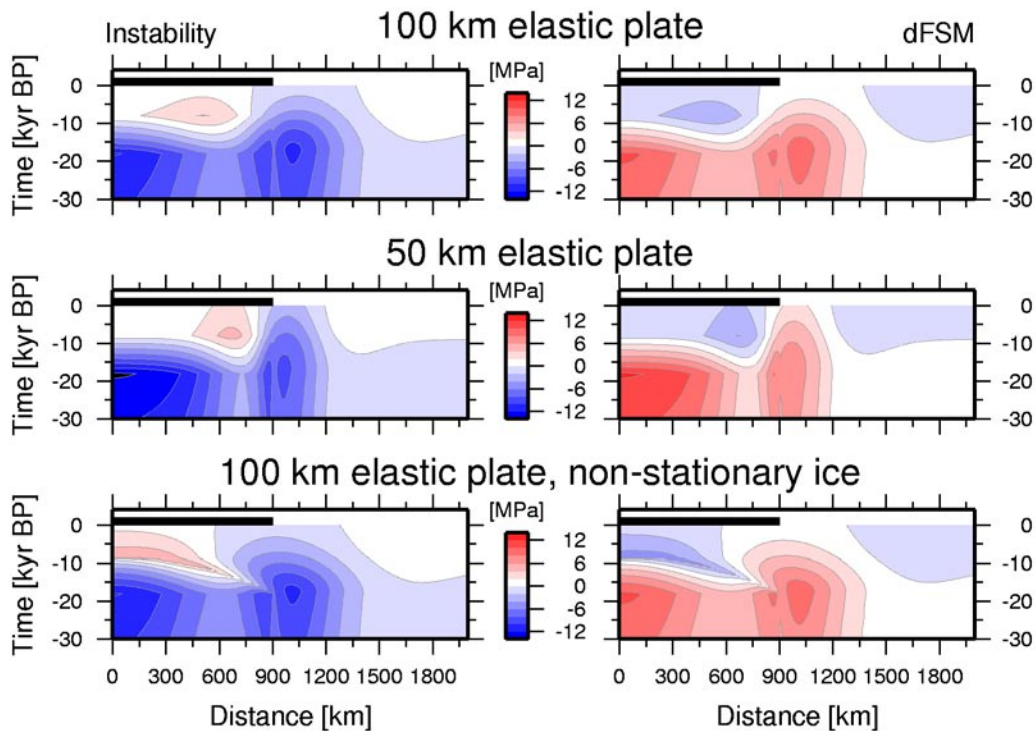
Figure 8-12. *Contour plots of Instability and dFSM for models m1, top, m2, middle, and m3, bottom. Note that the zero contour is between white and blue. Models include rebound stresses, overburden weight and a deviatoric component. Distance from the center of the ice load versus time, in kyr BP. The black bar on top of the plots indicate the extent of the ice at LGM.*

8.3 Mohr-Coulomb plasticity as a model material property

Our modelling software, Abaqus, allows for the implementation of Mohr-Coulomb plasticity as a material property. During execution, the model will be examined for plastic yielding and if the stress state is such that Mohr-Coulomb failure is activated, the material will relax the excess stress through plastic creep. This allows us to model fault failure in a more accurate manner since stresses can be relaxed, as occurs in the crust when the failure envelope is reached. As mentioned above, we have not yet implemented pore pressure effects into the model so in order to construct an initial state of stress in frictional failure equilibrium, we have to resort to very large differential stress. This modelling effort is currently work in progress and is not yet completely tested. In Figure 8-13 we show the result of using plasticity in Abaqus with an initial reverse state of stress in frictional equilibrium and without pore pressure. We limit the modelling to the models m1 and m3. We see in Figure 8-13 that the stability measures never reach the zero level under the ice load, the stresses have been relaxed by plastic creep. There is a region beyond the ice edge where the stability measures have passed the zero level, indicating that plasticity have not been activated in these areas. The reason for this behaviour is currently under investigation, as are the oscillations in model m3. We note that, as expected, the results in Figure 8-13 agree very well with those of Figure 8-12, the deviatoric initial state, and not with Figure 8-4 with zero initial stresses. The application of plasticity as a material property in the modelling will be very valuable for future modelling efforts.
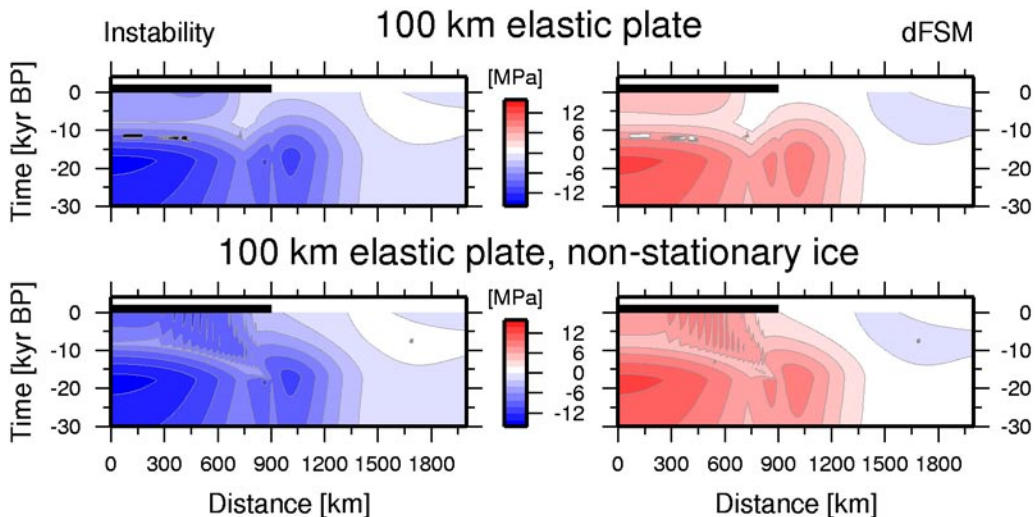
Figure 8-13. *Contour plots of Instability and dFSM for models m1, top, and m3, bottom. Note that the zero contour is between white and blue. Models include rebound stresses, overburden weight and a deviatoric component. Mohr-Coulomb plasticity is used as a material property in the modelling. Distance from the center of the ice load versus time, in kyr BP. The black bar on top of the plots indicate the extent of the ice at LGM.*

9   Summary and discussion

It is generally accepted that the large earthquakes that shook northern Scandinavia approximately 9,000 years ago and created fault scarps visible over hundreds of kilometer, sometimes more than 10 m high, were triggered by the deglaciation process. A quantitative description of the deglaciation process and its relation to fault stability has, however, been elusive. In this report we have studied a number of parameters involved in quantitative modelling of glacial isostatic adjustment (GIA) in order to illustrate how they affect stress, displacement and fault stability during deglaciation.

Using a variety of different reference models we have verified that our modelling approach, a finite element analysis scheme with proper adjustments for the requirements of GIA modelling, performs satisfactory. The size of the model and the density of the grid have been investigated in order to be able to perform high resolution modelling in reasonable time.

This report includes studies of both the ice and earth models. Naturally, the ice model describes the evolution of the load and thus dictates the effects of glaciation and deglaciation. We have seen that the steeper the ice edge is, the more concentrated is the deformation around the edge and consequently shear stress localizes with high magnitudes around the ice edge. Variations in the temporal evolution of both height and basal extent of the ice is very important for the response of the earth model and we have shown that the last stages of ice retreat can cause fault instability over a large lateral region.

In order to mimic the real Earth itself, an earth model can contain a very large number of parameters. We have chosen to investigate a few of these, which we have varied in the simplest ways possible. We have studied the effects of variations in stiffness, viscosity, density, compressibility and layer thickness on shear stress and vertical displacement. More complicated geometries such as multiple layers and lateral layer thickness variations have also been investigated. We generally find that these variations have more effect on the shear stress distributions than on the vertical displacement distributions. We also note that shear stress magnitude is affected more than the spatial shape of the shear stress distribution. Frequently, the variation of one parameter can be, in part, counteracted by the variation of another parameter, such that it would be very difficult to infer these parameters from limited data sets such as, e.g. vertical displacements only.

We chose to implement two variations on the Mohr-Coulomb failure criterion for our study of fault stability during glaciation/deglaciation. The Instability measure is the difference between the shear stress magnitude on a fault plane and the normal stress times the coefficient of friction and assesses how far from instability the fault is. The differential Fault Stability Margin, dFSM, /Wu and Hasegawa, 1996a/ is a relative measure which assesses whether or not a fault becomes more unstable when the stress state changes. We show that dFSM must be cautiously interpreted with respect to the initial state whereas Instability has a more direct interpretation. The Instability measure, however, is more vulnerable to erroneous assumptions of the actual values of e.g. the coefficient of friction and pore pressure. We also show that the initial state of stress is very important for the assessment of fault stability during glacial rebound.

This report highlights some important aspects that must be taken into consideration in future, more specific, modelling of fault stability in Scandinavia during deglaciation. A proper ice model, in terms of both ice thickness and temporal evolution, is, obviously, most important. The initial state of stress and pore pressure are variables that need careful consideration and are just as important as the earth model. Much of the earth model can be inferred from refraction seismic profiling and gravity/magnetic observations and modelling. The viscosity structure is a more delicate problem; a ductile lower crust, the strength of the lithospheric mantle and how to relate seismic lithospheric depths to equivalent elastic thicknesses are all issues that need consideration. We have seen interesting result in this report with regard to the ice models and the lateral variation of elastic plate thickness. A stationary ice edge will promote faulting closer to the edge at a different time than a receding ice. This could very well have bearing on the conditions during the Weichselian deglaciation, which was mostly stationary to the west but receded rapidly from the east and south. Western Scandinavia has a large variation in crustal and lithospheric thicknesses, from the thick interior of the Baltic shield, to the oceanic lithosphere off the coast of Norway. We saw in the models of lateral thickness variations that such rapid thinning causes sudden variations in the stress field which may be of importance for fault stability.

Bibliography

Amelung F, Wolf D, 1994. Viscoelastic perturbations of the Earth: significance of the incremental gravitational force in models of glacial isostacy, Geophys. J. Int., 117, 864–879.

Bott M H P, Kusznir N J, 1984. The origin of tectonic stress in the lithosphere, Tectonophysics, 105, 1–13.

Byerlee J D, 1978. Friction of rocks, Pure Appl. Geophys., 116, 615–626.

Cadek O, 2003. Viscoelastic relaxation of spherical earth with a 3D viscosity structure, Geophys. Res. Abs., 5, 05279, EGS, Nice.

Dziewonski A M, Anderson D L, 1981. Preliminary reference Earth model, Phys. Earth Planet. Inter., 25, 297–356.

Farrell W E, Clark J A, 1976. On postglacial sea level, Geophys. J. R. astro. Soc., 46, 647–667.

Forsyth D, Uyeda S, 1975. On the relative importance of the driving forces of plate motion, Geophys. J. R. astr. Soc., 43, 163–200.

Gasperini P, Sabadini R, 1989. Lateral heterogeneities in mantle viscosity and post-glacial rebound, Geophys. J., 98, 413–428.

Inovecky L, 2003. Postglacial relaxation of the Earth's Models in cylindrically symmetric geometry. Masters thesis, Charles University, Prague, Czech Republic.

Jaeger J C, Cook G W, 1979. Fundamentals of rock mechanics, Chapman and Hall, London, 593 pp.

James T S, Bent A L, 1994. A comparison of eastern North American seismic strain rates to glacial rebound strain-rates, Geophys. Res. Lett., 21, 2,127–2,130.

Johnston A C, 1987. Suppression of earthquakes by large continental ice sheets, Nature, 330, 467–469.

Johnston A C, 1989. The effect of large ice sheets on earthquake genesis, in Earthquakes at North Atlantic Passive Margins: Neotectonics and Postglacial Rebound, edited by S. Gregersen and P. Basham, pp 581–599, Kluwer, Dordrecht.

Johnston P, Wu P, Lambeck K, 1998. Dependence of horizontal stress magnitude on load dimension in glacial rebound models, Geophys. J. Int., 132, 41–60.

Kaufmann G, Johnston P, 1997. Benchmark comparisons for model of glacial isostatic adjustment, http://rses.anu.edu.au/geodynamics/GIA_benchmark/, Research School of Earth Sciences, Australian National University, Canberra, Australia.

Kaufmann G, Wu P, Wolf D, 1997. Some effects of lateral heterogeneities in the upper mantle on postglacial land uplift close to continental margins. Geophys. J. Int., 128, 175–187.

Kaufmann G, Wu P, Li G, 2000. Glacial isostatic adjustment in Fennoscandia for a laterally heterogeneous earth, Geophys. J. Int., 143, 262–273.

Kaufmann G, Wu P, 2002. Glacial isostatic adjustment on a three-dimensional earth: examples from Fennoscandia and the Barents Sea, in Sea-level, Crustal Deformation, Gravity and Rotation, edited by J. Mitrovica and L. Vermeersen, AGU Geodynamics Series, pp 1–7, AGU.

Klemann V, Wolf D, 1998. Modelling of stresses in the Fennoscandian lithosphere induced by Pleistocene glaciations, Tectonophysics, 294, 291–303.

Klemann V, Wolf D, 1999. Implications of a ductile crustal layer for the deformation caused by the Fennoscandian ice sheet, Geophys. J. Int., 139, 216–226.

Klemann V, Wu P, Wolf D, 2003. Compressible viscoelasticity: stability of solutions for homogeneous plane earth models, Geophys. J. Int., 153, 569–585.

Klemann, 2004. Personal communication.

Kujansuu R, 1964. Nuorista siirroksista Lappissa. Summary: Recent faults in Lapland, Geologi, 16, 30–36.

Kusznir N J, 1991. The distribution of stress with depth in the lithosphere: thermo-rheological and dynamic constraints, In: Whitmarsh, R.B. (Ed.), Tectonic Stress in the Lithosphere, Royal Society, London, pp 95–107.

Lagerbäck R, 1979. Neotectonic structures in northern Sweden, Geol. Fören. Stockholm Förh., 100, 263–269.

Lambeck K, Smither C, Johnston P, 1998a. Sea-level change, glacial rebound and mantle viscosity for northern Europe, Geophys. J. Int., 134, 102–144.

Lambeck K, Smither C, Ekman M, 1998b. Tests of glacial rebound models for Fennoscandinavia based on instrumented sea- and lake-level records, Geophys. J. Int., 135, 375–387.

Latychev K, Mitrovica J X, Tromp J, Komatitsch D, Tamisiea M, 2003. Glacial isostatic adjustment on aspherical earth models: Results from a new finite element formulation, Geophys. Res. Abs., 5, 07569, EGS, Nice.

Lund B, Slunga R, 1999. Stress tensor inversion using detailed microearthquake information and stability constraints: Application to Ölfus in southwest Iceland, J. Geophys. Res., 104, 14,947–14,964.

Milne G A, Mitrovica J X, Davis J L, 1999. Near-field hydro-isostacy: The implementation of a revised sea-level equation, Geophys. J. Int., 139, 464–482.

Milne G A, Mitrovica J X, Scherneck H-G, Davis J L, Johansson J M, H Koivula, Vermeer M, 2004. Continuous GPS measurements of postglacial adjustment in Fennoscandia: 2. Modeling results, J. Geophys. Res., 109, B02412, doi: 10.1029/2003JB002619.

Mitrovica J X, Davis J L, Shapiro I I, 1994a. A spectral formalism for computing three-dimensional deformations due to surface loads 1. Theory, J. Geophys. Res., 99, 7,057–7,073.

Mitrovica J X, Davis J L, Shapiro I I, 1994b. A spectral formalism for computing three-dimensional deformations due to surface loads 2. Present-day glacial isostatic adjustment, J. Geophys. Res., 99, 7,075–7,101.

Mitrovica J X, G A Milne, J L Davis, 2001. Glacial isostatic adjustment on a rotating Earth Geophys. 3. Int. vol 147, p 562–578.

Olesen O, 1988. The Stuoragurra Fault, evidence of neotectonics in the Precambrian of Finnmark, northern Norway, Norsk Geologisk Tidsskrift, 68, 107–118.

Peltier W R, 1974. The impulse response of a Maxwell Earth, Rev. Geophys. Space Phys., 12, 649–669, .

Quinlan G, 1984. Postglacial rebound and the focal mechanisms of eastern Canadian earthquakes, Ca. J. Earth Sci., 21, 1,018–1,023.

Sabadini R, Yuen D A, Portney M, 1986. The effects of upper-mantle lateral heterogeneities on post glacial rebound, Geophys. Res. Lett., 13, 337–340.

Stein S, Sleep N H, Geller R J, Wang S C , Kroeger G C, 1979. Earthquakes along the passive margin of Eastern Canada, Geophys. Res. Lett., 6, 537–540.

Townend J, Zoback M D, 2000. How faulting keeps the crust strong, Geology, 28, 399–402.

Tushingham A M, Peltier W R, 1991. Ice 3G: A new global model of Late Pleistocene deglaciation based upon geophysical predictions of post-glacial relative sea-level change, J. Geophys. Res., 96, 4,497–4,523, .

Walcott R I, 1970. Isostatic response to loading of the crust in Canada, Can. J. Earth sci., 7, 716–727.

Wallroth T, Ericsson L O, Hernelind J, 2002. Benchpar WP 4 / Decovalex III, BMT3, Phase I, Progress Report, Dep. of Geology, Chalmers University of Technology, Göteborg.

Wolf D, 1985. On Boussinesq's problem for Maxwell continua subject to an external gravity field, Geophys. J. R. astr. Soc., 80, 275–279.

Wolf D, 1991. Viscoelastodynamics of a stratified, compressible planet: incremental field equations and short- and long-time asymptotes, Geophys. J. Int., 104, 401–417.

Wolf D, 1993. The changing role of the lithosphere in models of glacial isostacy: a historical review, Global Planet. Change., 8, 95–106.

Wu P, 1992. Deformation of an incompressible viscoelastic flat earth with power-law creep: a finite element approach, Geophys. J. Int., 108, 35–51.

Wu P, 1993. Post-glacial rebound in a power-law medium with axial symmetry and the existence of the transition zone in relative sea level data. Geophys. J. Int., 114, 417–432.

Wu P, 1997. Effect of viscosity structure on fault potential and stress orientations in eastern Canada, Geophys. J. Int., 130, 365–382.

Wu P, 2004. Using commercial finite element packages for the study of earth deformations, sea levels and the state of stress, Geophys. J. Int., 158, 401–408.

Wu P, Hasegawa H S, 1996a. Induced stresses and fault potential in eastern Canada due to a disc load: a preliminary analysis, Geophys. J. Int., 125, 415–430.

Wu P, Hasegawa H S, 1996b. Induced stresses and fault potential in eastern Canada due to a realistic load: a preliminary analysis, Geophys. J. Int., 127, 215–229.

Wu P, Johnston P, 2000. Can deglaciation trigger earthquakes in N. America? Geophys. Res. Lett., 27, 1,323–1,326.

Wu P, Ni Z, 1996. Some analytical solutions for the viscoelastic gravitational relaxation of a two-layer non-self-gravitating incompressible spherical earth. Geophys. J. Int., 126, 413–436.

Wu P, Peltier W R, 1982. Viscous gravitational relaxation, Geophys. J. R. astro. Soc., 70, 435–485.

Wu P, van der Wal W, 2003. Postglacial Sealevels on a Spherical, Self-gravitating Viscoelastic Earth: Effects of lateral viscosity variations in the upper mantle on the inference of viscosity contrasts in the lower mantle, Earth and Planet. Sci. Lett., 211, 57–68.

Wu P, Ni Z, Kaufmann G, 1998. Postglacial rebound with lateral heterogeneities: from 2D to 3D modelling, in Dynamics of the Ice Age Earth: A Modern Perspective, edited by P. Wu, pp 557–582, Trans Tech. Pub., Zürich, Switzerland.

Wu P, Johnston P, Lambeck K, 1999. Postglacial rebound and fault instability in Fennoscandia, Geophys. J. Int., 139, 657–670.

Zoback M D, Townend J, 2001. Implications of hydrostatic pore pressures and high crustal strength for the deformation of intraplate lithosphere, Tectonophysics, 336, 19–30.

Zoback M L, 1992. First- and second-order patterns of stress in the lithosphere: The World Stress Map Project, J. Geophys. Res., 97, 11,703–11,728.